Acta Materialia 212 (2021) 116933

Contents lists available at ScienceDirect

Acta Materialia

journal homepage: www.elsevier.com/locate/actamat

Influence of microstructure and atomic-scale chemistry on the direct reduction of iron ore with hydrogen at 700°C

Se-Ho Kim[a,1], Xue Zhang[a,c,1], Yan Ma[a,1], Isnaldi R. Souza Filho[a], Kevin Schweinar[a], Katja Angenendt[a], Dirk Vogel[a], Leigh T. Stephenson[a], Ayman A. El-Zoka[a], Jaber Rezaei Mianroodi[a], Michael Rohwerder[a], Baptiste Gault[a,b,**], Dierk Raabe[a,*]

[a] Max-Planck-Institut für Eisenforschung, Max-Planck-Straße 1, Düsseldorf 40237, Germany
[b] Department of Materials, Imperial College, South Kensington, London SW7 2AZ, United Kingdom
[c] Corrosion Center, Institute of Metal Research, Chinese Academy of Sciences, Shenyang 110016, China

ARTICLE INFO

Article history:
Received 23 October 2020
Revised 25 February 2021
Accepted 23 April 2021
Available online 26 April 2021

ABSTRACT

Steel is the most important material class in terms of volume and environmental impact. While it is a sustainability enabler, for instance through lightweight design, magnetic devices, and efficient turbines, its primary production is not. Iron is reduced from ores by carbon, causing 30% of the global CO_2 emissions in manufacturing, qualifying it as the largest single industrial greenhouse gas emission source. Hydrogen is thus attractive as alternative reductant. Although this reaction has been studied for decades, its kinetics is not well understood, particularly during the wüstite reduction step which is much slower than hematite reduction. Some rate-limiting factors of this reaction are determined by the microstructure and local chemistry of the ores. Here, we report on a multi-scale structure and composition analysis of iron reduced from hematite with pure H_2, reaching down to near-atomic scale. During reduction a complex pore- and microstructure evolves, due to oxygen loss and non-volume conserving phase transformations. The microstructure after reduction is an aggregate of nearly pure iron crystals, containing inherited and acquired pores and cracks. We observe several types of lattice defects that accelerate mass transport as well as several chemical impurities (Na, Mg, Ti, V) within the Fe in the form of oxide islands that were not reduced. With this study, we aim to open the perspective in the field of carbon-neutral iron production from macroscopic processing towards better understanding of the underlying microscopic transport and reduction mechanisms and kinetics.

1. Introduction and motivation

Steel is by far the most important metallic material, both in terms of quantity and the breadth of industrial applications, ranging from transportation, infrastructure, construction, machinery to safety. It is also an enabler of clean energy conversion technologies, such as wind or solar thermal. Steel can be recycled practically infinitely by collecting and re-melting scraps. When averaged over all steel grades and scrap types its global recycling rate is about 70%, making steel the world's most recycled material, and, in absolute tonnage, amounting to more than all other recycled materials combined [1–3]. However, due to steel's global role as a backbone material of economic development and its high and steady growth rates, scrap-based secondary synthesis alone cannot satisfy the global demand. Also, a major challenge in using large amounts of scrap to produce high grade steel lies in the gradual accumulation of undesired tramp elements such as copper. Therefore, fresh iron from ore reduction will always be needed in addition to scrap recycling. For these reasons, huge quantities of iron are produced each year by conventional primary synthesis, via reduction of iron ores in blast furnaces, using carbon as a reductant [4]. The current annual consumption of iron ores for this process amounts to a gigantic 2.6 billion tons, producing about 1.28 billion tons of pig iron through this route [5]. Each ton of steel produced by this conventional primary synthesis, i.e. through a blast furnace followed by a basic oxygen converter, creates about 2.1 tons of CO_2. Currently, more than 70% of the global iron production is made through this process route [4].

* Corresponding author.
** Corresponding author at: Max-Planck-Institut für Eisenforschung, Max-Planck-Straße 1, Düsseldorf 40237, Germany.
E-mail addresses: b.gault@mpie.de (B. Gault), d.raabe@mpie.de (D. Raabe).
[1] These authors contributed equally to this work.

https://doi.org/10.1016/j.actamat.2021.116933
1359-6454/

These numbers make steel one of the most staggering single sources of greenhouse gas on the planet, with about 6.5% of all CO_2 emissions, i.e. 30% of all CO_2 emissions from the manufacturing sector [1]. Global growth rate projections suggest a massive further increase of these emissions at least up to the year 2050 if no technology changes are implemented.

However, unreflected CO_2 sequestration may also produce negative impacts [6–10]. For instance, the currently developed approach of underground CO_2 storage for long-term periods (i.e. virtually hundreds or thousands of years) is a technique that might cause harmful effects on soil and water due to leakage [11]. Therefore, three engineering strategies are currently being explored to mitigate this dramatic contribution of primary iron synthesis to global warming.

The first one is an increase in recycling. However, secondary production of steel still causes between 0.3 and 0.6 ton CO_2 per ton of recycled steel, due to the use of graphite electrodes in the electric arc furnaces, injected fuels and the electrical power which is mostly generated from fossil fuels. Also, there is simply not enough scrap available (globally only about 1/3 of the total production comes from such secondary resources) to cover the total demand, due to the longevity of many steel products, for instance, in buildings, machines and vehicles [12]. More than 3/4 of all steel products that were ever made are still in use today. Some steel constructions and buildings have been lasting for 150 years, for instance the Brooklyn Bridge.

The second scenario is the use of electrolysis, similar to the primary production of aluminum via the Hall-Heróult process [13]. However, the iron oxide's high melting point and the chemically aggressive nature of the high-temperature liquid salts make this processing route currently less attractive for commercial production. Promising in this field, however, is the recent progress in low-temperature electrolysis, using ionic liquids as solvents [[14],[15]].

The third, and currently most viable alternative, lies in the use of hydrogen as a reducing agent (instead of carbon), provided it comes from sustainable sources [16]. Hydrogen-based reduction schemes need to consider three thermodynamic constraints in the design of reactors. (1) The net energy balance for the complete reduction of iron oxide to iron with hydrogen is endothermic, i.e. it requires external energy to proceed [16], whereas it is exothermic with carbon monoxide. (2) In many of the current transition techniques for the reduction of iron ores, hydrogen is not used as the only reductant, but it can be mixed with several types of carbon carriers in the same reactor [[17],[18]]. This means that the catalytic splitting of the injected molecular dihydrogen into reactive atomic hydrogen ($H_2 \leftrightarrow 2H$) and its reaction with the oxide competes with other reduction reactions [16]. Also, the reaction product, i.e. water, must be removed from the reaction zone as it can re-oxidize or block the reduction front. This is a challenging detail as water or, respectively, the oxygen that is removed from the oxide, desorbs and diffuses only slowly compared with the atomic reductants. High partial pressure of water has indeed been shown to act detrimental to the nucleation and growth of iron on wüstite surfaces [[19],[20]]. (3) The availability of green hydrogen (made from sustainable sources) is currently by far too small to mitigate the steel industry's greenhouse gas output. This means that the reduction via gray hydrogen has to serve as transition technology with a reduced mitigation effect [[21],[22]]. Gray hydrogen, which makes currently more than 95% of the global hydrogen market, comes from steam reforming and partial oxidation of methane, coal gasification and wet coke gas production. Hydrogen won from reforming contains CO as a contaminant, an effect which must be considered in the carbon balance of downstream reactions. A more sustainable alternative to producing large amounts of hydrogen for iron ore reduction might come from methane pyrolysis, where solid carbon is the byproduct.

2. Approaches to hydrogen-based reduction of iron oxide and the role of microstructure

The hydrogen-based reduction scenario with the currently highest technology-readiness level is to inject hydrogen into existing blast furnaces, in addition to coke [14]. The coke lends the furnace its permeable structure. This structure is needed to allow gas percolation as well as slag and metal outflux [16]. Current pilot operations use either gray hydrogen (from gas reforming) or coke gas. The latter is a mixture containing up to 65% hydrogen and more than 20% methane, available in integrated steel factories from the coke plant [[23],[24]].

Yet, the underlying microscopic processes and some aspects associated with the basic thermodynamics and kinetics within the blast furnace are not well understood and can thus not be controlled or tuned for higher reduction efficiency and improved CO_2 balance. A possible consequence of this is that the injected hydrogen partially evades without contributing much to the reduction reaction and thus without markedly reducing CO_2 emissions, even though hydrogen diffuses and percolates much faster than CO and CO_2. Another efficiency limit is that the reaction is endothermic, hence, more carbon-carriers are required to keep the temperature high enough when increasing the hydrogen amount injected.

The second technology option is the direct reduction of solid iron ore pellets by hydrogen at temperatures above 570 °C [[21],[25],[26]]. In this case, the reduction proceeds from hematite (Fe_2O_3) to magnetite (Fe_3O_4), and further to wüstite (FeO) and metallic iron (Fe).

Several macroscopic studies exist on the reduction of iron oxide exposed to different gas mixtures (in part including hydrogen) in the temperature range of 500–900 °C [27–30]. However, several key aspects that influence the reduction kinetics in terms of the microstructure, nano-chemistry, porosity, interface fracture, and mechanics of the ores and partially reduced products have not been studied. These less-known parameters and mechanisms have in common that they act on micro- and even near-atomic length scales, with substantial influence on transport and reaction kinetics. Thus, the next level of insight into the carbon-free reduction of iron ores requires direct observations at these small scales, probing both, structure and chemistry. Better understanding of these processes would enable the design of suited ore pellets and process conditions with respect to ore preparation, pre-processing, enrichment strategies, microstructure, dispersion, porosity, grain size, texture, thermo-mechanical conditions, and chemical composition regarding the pellets, as well as reduction gas mixtures and reactor design.

3. Experimental set-up and global kinetics of reduction of hematite with hydrogen

For studying the influence of microstructure on the hydrogen-based reduction of iron ore pellets, we conducted a multiscale investigation of an isothermal reduction of commercial hematite direct reduction pellets (8 mm pellet size; 0.36 wt.% FeO, 1.06 wt.% SiO_2, 0.40 wt.% Al_2O_3, 0.73 wt.% CaO, 0.57 wt.% MgO, 0.19 wt.% TiO_2, 0.23 wt.% V, 0.10 wt.% Mn as well as traces of P, S, Na, K), exposed to pure hydrogen at 700 °C in a static bed, using electron microscopy, secondary electron imaging (SE), electron backscatter diffraction (EBSD), electron channeling contrast imaging (ECCI) and atom probe tomography (APT). Reference experiments were also conducted on pure wüstite single crystals, with the aim to understand microstructure evolution during the later reduction stages without inherited pores or cracks from preceding processing and reduction steps.

The EBSD analysis in this system is challenging owing to the crystallographic similarity between magnetite and wüstite. The

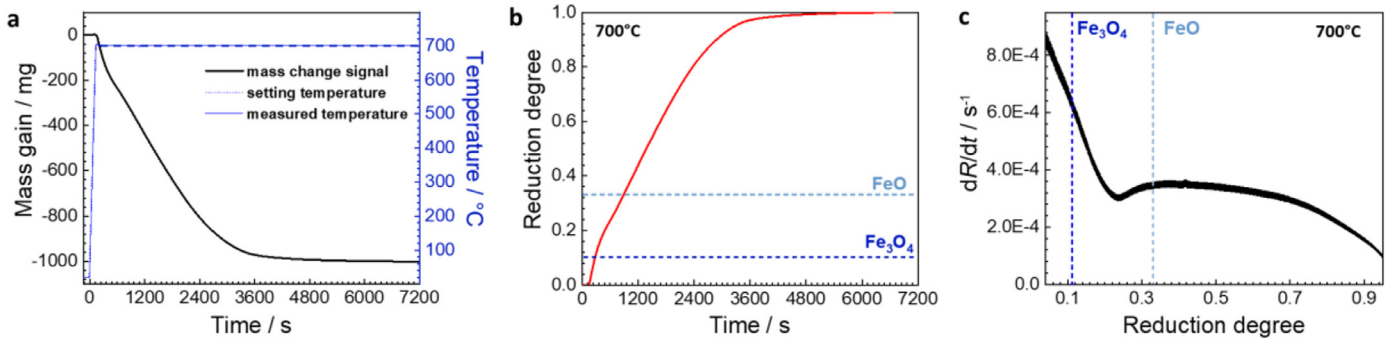

Fig. 1.. Reduction kinetics of hematite ore pellets reduced in hydrogen at 700 °C at a gas flow rate of 30 L/h. (a) Mass change and temperature vs. time. (b) Reduction degree (normalized values from (a)) vs. time. The dotted lines at 0.11 and 0.33 are the theoretical reduction degrees for a complete reduction from Fe_2O_3 to Fe_3O_4 and Fe_3O_4 to FeO, respectively. (c) Reduction rate vs. reduction degree. The end of the abrupt slope between 0.11 and 0.15 reduction degree marks the end of the first stage of the reduction. It is characterized by the fast transition from Fe_2O_3 to Fe_3O_4 and the subsequent stage of decelerating reduction rates roughly ends at the local minimum of ~0.23, indicating the Fe_3O_4 to FeO transition regime. The further reduction of the FeO into Fe becomes then the rate-limiting process.

hematite (Fe_2O_3) has a trigonal crystal structure and can be readily distinguished in EBSD from the other two oxide phases which are cubic. Yet, both, magnetite (Fe_3O_4) and wüstite (FeO) have a face-centered-cubic (fcc) crystal structure. This crystallographic similarity makes indexing their Kikuchi diffraction patterns ambiguous. When choosing default EBSD settings for structure files, it is not readily possible to distinguish these phases. Therefore, the reflections in the structure files and the indexing parameters must be optimized for the differentiation of the EBSD patterns. In particular, the reflection line pertaining to the {311} plane family must be included in the structure files for identifying magnetite, but it is not required for identifying wüstite. This adjustment enables the proper differentiation of magnetite from wüstite during EBSD data acquisition and microstructure reconstruction.

Fig. 1a shows the mass change of a hematite ore pellet during its reduction in pure dihydrogen at 700 °C under a constant gas flow rate of 30 L/h. The reduction degree is shown in Fig. 1b. The reduction rate (quantified as mass loss per time) drops fast in the initial stage, slows down after approx. 2400 s and reaches completion after approx. 6000 s. More specifically, Fig. 1c shows the reduction rate as a function of the fraction of reduced material, allowing better separation of the kinetic stages in such gas-solid reactions [[16],[31]]. Fig. 1b and c summarize the different steps in the reduction process from Fe_2O_3 (hematite) to Fe_3O_4 (magnetite) to FeO (wüstite) and finally to α-Fe (α-iron, bcc). One should note in that context that wüstite is not a stoichiometric compound (yet, for simplicity written FeO hereafter) but a defected pseudophase which can be chemically described as $Fe_{(1-x)}O$, where X varies at 700 °C between about 0.90 and to 0.97 at ambient pressure [32–37].

The dotted lines at the reduction degree of 0.11 and 0.33 indicate the stoichiometry pertaining to the complete reduction from Fe_2O_3 to Fe_3O_4 and Fe_3O_4 to FeO, respectively. The observed reduction sequence agrees with the previous literature on the hydrogen-based hematite reduction at temperatures above 570 °C [16].

The global kinetic data show that the reduction rate initially decreases very rapidly, going through a local minimum (at a reduction degree of ~0.23) and then enters into a sigmoidal shape. The first stage with its rapid decay ends between 11 and 15% of the overall reduced material. As suggested by stoichiometry, this transition region marks the end of the first stage in reduction, namely, the reduction $Fe_2O_3 \rightarrow Fe_3O_4$. The subsequent stage, characterized by a steep yet decaying reduction rate corresponds to the transition from Fe_3O_4 to FeO. The mass change at the end of the Fe_3O_4 to FeO transition overlaps with the onset of the FeO → Fe reaction. We assume, that at the local minimum, the mass loss due to the FeO→Fe transition is more dominant than that of the $Fe_3O_4 \rightarrow$ FeO transition, after which the sluggish reduction of the FeO becomes the prevalent process.

These findings about the global reduction kinetics from hematite to bcc iron and the suggested sequence of reduction stages observed in our study are similar to earlier observations [[27],[37–45]]. For example, Wagner et al. [46] found the same sequence in reduction stages by using thermogravimetry, X-ray diffraction, SEM and Mössbauer spectrometry. Zieliński et al. [37] investigated the reduction kinetics by exposing hematite to mixtures of water and hydrogen. They reported that for the case of a water-to-hydrogen ratio above 0.35 the reduction of hematite proceeds in three steps, namely,$Fe_2O_3 \rightarrow Fe_3O_4 \rightarrow$ FeO → Fe and in two steps, namely, $Fe_2O_3 \rightarrow Fe_3O_4 \rightarrow$ Fe for atmospheric ratios below that value. This means that for high hydrogen partial pressures they found the same reduction sequence as observed in this study.

Pineau and co-workers studied the reduction of hematite and magnetite across a wide temperature range [[39],[40]], with the aim to identify the rate-controlling processes. They suggested that the first reduction step, viz., from hematite to magnetite with hydrogen gas has an apparent activation energy of 76 kJ/mol and the one from magnetite to iron of 88 and 39 kJ/mol, for temperatures below and above 420 °C, respectively. By using analytical rate models they concluded that the reaction rate was controlled by two- and three-dimensional growth of nuclei and by phase boundary reactions at temperatures lower and higher than 420 °C, respectively. They observed formation of compact iron layers during the reduction of hematite above 420 °C. They and several other authors also found that the total reduction rate of hematite with hydrogen was systematically higher than that observed for CO-based reduction [31]. For other temperatures and when using magnetite (instead of hematite) as a starting oxide they found slightly different apparent activation energies.

Piotrowski et al. [[47],[48]] studied the kinetics of hematite to magnetite and further to wüstite reduction by means of thermogravimetry in the temperature range between 700 and 900 °C. They interpreted their experimental data in terms of simulation results obtained by an Avrami-Erofeev model (which is a homogenized mean-field formulation for nucleation and growth) for the initial stages of the reduction process and coupled diffusion equations for the final stages of the reduction process. They concluded that the initial stage is controlled by nucleation (of magnetite or wüstite, respectively) and 1D growth at the gas/iron oxide interface and the latter stages are characterized by a shift towards diffusion control.

Our present data, specifically the decelerating shape for the first two reduction steps $Fe_2O_3 \rightarrow Fe_3O_4 \rightarrow$ FeO indicate that they

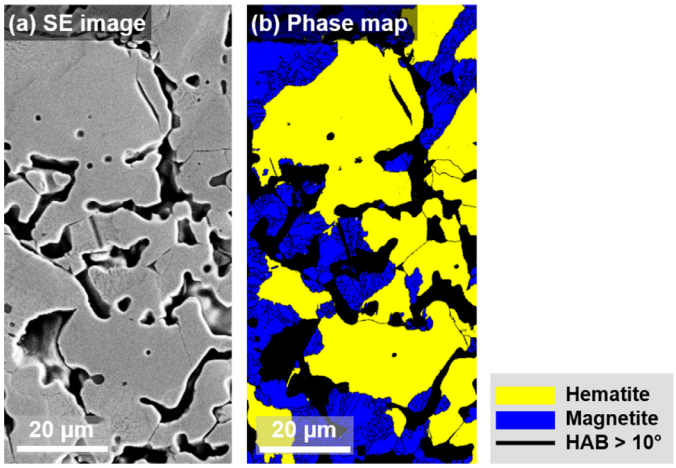

Fig. 2. Microstructure of a region inside of the pellet (taken about 2 mm below the pellet surface) imaged by using SEM and EBSD characterization after partial reduction at 700 °C for 1 min under a H_2 flux of 30 L/h: (a) SEM image, (b) EBSD phase map together with high angle grain boundaries (HAB).

are predominantly controlled by diffusion or / and by the phase-boundary reaction [[10],[23]]. In the former case, transport of reactants to or – here more likely – products away from the reaction interface are the rate-determining steps. In the latter case, the reaction process itself and the motion of the reaction interface with progressing reaction are the limiting factors [17]. The latter view is in line with the interpretation of Wang et al. [49], who investigated the reduction kinetics of Fe_2O_3 (size of 100–200 μm) with CO and found that both the $Fe_2O_3 \rightarrow Fe_3O_4$ and $Fe_3O_4 \rightarrow FeO$ reduction processes were rate-determined by the phase-boundary reaction and less by transport effects.

Bonalde et al. [26] studied the direct reduction of Fe_2O_3 pellets with both, high porosity and high inter-pore connectivity, through hydrogen-carbon monoxide gas mixtures. They used an analytical approach, referred to as 'grain model', to interpret and simulate the observed kinetics for a scenario with a reduction at 850 °C using hydrogen and carbon monoxide. The reduction kinetics was experimentally tracked by weight loss measurements. The model considered the grain particles' diameters and the porosity of the hematite pellets. They concluded that for the case of hydrogen and carbon monoxide fueled reduction processes, the chemical interface reactions and the diffusion of the internal gas species acted as competing processes during the first stage of the reduction, and the internal gas diffusion as a rate-controlling step during the last stage of the process. One assumption of the model by Bonalde et al. [26] is that the phase boundary is moving towards the center of the pellet. In this model such pellets are assumed to be compact and homogeneous. However, the assumption of pellet homogeneity is not quite in agreement with the findings in our study, where we instead observe that the phase boundaries are scattered inside of the pellet, forming a complex microstructure together with multiple defects and pores, (Fig. 2), yet, with a global volume and frequency gradient between surface and center. This gradient in the occurrence of phase boundaries is characterized by a decrease in the transformation rate from the readily transformed near-surface regions towards the less transformed center regions of the pellet yet, with many scattered transformation zones in all the layers. Hence, we assume that the kinetics of the iron ore reduction during the first stages is in our case most likely diffusion-controlled. Details of these gradients in microstructure and reaction kinetics through the thickness of the gradients will be discussed in the ensuing sections.

As the onset of the FeO → Fe transition overlaps with the end of the $Fe_3O_4 \rightarrow FeO$ transition (Fig. 1c), it is difficult to define in our case whether the wüstite reduction step itself is during the initial stage sigmoidally-shaped or deceleratory-shaped [46].

Literature reports discuss the reduction of (mostly compact and dense) wüstite specimens essentially in terms of three stages, viz., oxygen depletion of the wüstite, Fe nucleation and growth of Fe [[32],[33]].

The kinetics of the first step, namely, the gradual removal of oxygen from the slightly under-stoichiometric wüstite [[50],[51]] depends on the outbound diffusion length of the oxygen towards internal or outer free surfaces. This in turn depends on the inherited and on the reduction-acquired pore structure. This means that originally dense iron oxide samples with no inherited pores and/or low connectivity have longer diffusion lengths for oxygen than material that has a high pore and fracture content. The oxygen depletion leads likely to first nanoscale Fe clusters, introducing stage two of the wüstite reduction kinetics. The occurrence of the first Fe clusters will be influenced by the microstructure of the material, i.e. leading for instance to preferred formation of Fe nuclei at grain boundaries. For instance, Bahgat et al. [52–54] studied the iron nucleation process in wüstite exposed to different reduction gas mixtures and observed an influence of the grain boundaries and of the grain orientations using EBSD. They found that the number of iron nuclei that had formed near grain boundaries was much larger than that in the grain interiors. They interpreted this preference of iron nucleation at defects in terms of faster transport of vacancies and divalent Fe cations via surface and grain boundary diffusion. Similar observations of Fe surface nucleation were also made by Moujahid and Rist [55], who described this stage in terms of the nucleation and surface growth of iron.

Nicholle and Rist [56] studied the growth of iron whiskers on wüstite and interpreted it in light of Wagner's theory for the reduction of nonstoichiometric oxides [57]. The term whisker is in this context used for tiny iron crystals that protrude from the oxide and grow normal to the surface with a longitudinal shape. They are of importance for both, studying the nucleation of Fe in wüstite and for understanding sticking among partially reduced wüstite particles. In Wagner's approach [57] the first nucleus of Fe develops if its accumulation in the supersaturated wüstite is sufficiently uniform [32]. Nicholle and Rist [56] cast this argument into a model where such Fe agglomeration inside wüstite prior to nucleation is expressed in terms of the reaction constant, the chemical diffusion coefficient of Fe, the particle radius, the Fe/O ratio at equilibrium with the gas, and the critical Fe/O ratio for nucleation at the most favorable sites, for instance at internal interfaces or other defects.

The groups of Hayes et al. [[50],[58],[59]], Turkdogan et al. [[27],[60],[61]] and Gleitzer et al. [[30],[62],[63]] classified the Fe product morphologies that formed during hematite and wüstite reduction into three types of porous Fe, porous wüstite covered with dense Fe layers and dense wüstite covered with dense Fe layers, depending on the relative rates of the chemical reaction with the gas and the mass transport processes both in and on the solid.

After the nucleation of Fe in the wüstite the third and last stage of the reduction consists in the slow growth of Fe layers around the remaining wüstite, where the growth morphology of Fe depends substantially on both, the inherited and reduction-acquired microstructure of the wüstite as well as on its chemical purity [[50],[59],[64]]. Of specific importance for the overall kinetics during this last stage is the connectivity, compactness and defect state of the Fe layers that form around the shrinking wüstite [[51],[60]]. If the Fe forms a closed layer and is devoid of defects (such as interfaces, pores and cracks) the outbound oxygen diffusion is drastically slowed down [65–67] while a higher degree of fracture and porosity allow for much faster surface diffusion of oxygen ions

from the reaction front with the wüstite to the outer surface of the Fe, where they can recombine with hydrogen to form water [58].

This means that wüstite reduction into iron can be a nucleation-controlled process [23], particularly during the initial stages, or a more oxygen diffusion-controlled process, particularly during the later stages, depending on the microstructural defect population and its percolation features inside the freshly formed iron layers.

This kinetic interpretation is plausible as the Fe_2O_3 to Fe_3O_4 reduction as well as the Fe_3O_4 to FeO reduction only stand for modest stoichiometric O losses of 1/9 and 1/4 units of O, respectively, whereas in the final reduction step from wüstite to iron, FeO loses a full unit of O [[35],[68],[69]]. Thus, the compositional and structure fluctuations required for nucleation of Fe inside the FeO are larger than those required for the preceding reduction steps. In such a case, the nucleation of iron might be the rate-limiting step in the initial stage of the wüstite reduction.

It should be noted that the plot of the conversion rate against conversion degree for the wüstite reduction process (Fig. 1c) after a reduction degree of ~0.23 does not exactly follow a sigmoidal shape, but it has a plateau region starting at around 0.3–0.45 reduction degree, Fig. 1c. This feature indicates that even if the beginning of the reaction is determined by the Fe nucleation rate, another important factor, most likely diffusion, should have a significant influence on the kinetics particularly during the last stage of the FeO → Fe transition. This matches the kinetic picture behind most of the existing rate models which have considered both, the nucleation and nuclei growth phase and the diffusion through the expanding Fe layers, see e.g. [[37],[45],[49],[58],[69–71]].

Irrespective of this agreement in the basic global reaction sequence, there is no clear picture yet on the possible roles of specific microstructural factors such as the size and porosity of the iron ore particles, and the difficulty in differentiating the overlapping kinetic signals among some of the reaction stages. Thus, to gain better insight into the rate-determining mechanisms of the reduction process, the kinetic steps at certain reduction stages have to be elucidated in higher microstructural and chemical detail.

From a mean-field perspective, the reduction from wüstite can be essentially classified into two extreme scenarios, namely, one before and one after the formation of a continuous Fe layer on top of the wüstite. When the H_2 reductant gas is in direct contact with the iron oxide, the kinetic steps of the reduction process can be summarized as follows [72]: (1) H_2 molecules diffuse to the surface and (2) react with the oxygen ions from the external surface of the iron oxide, forming water and electrons part of which reduce Fe^{3+} to Fe^{2+} via the equation $Fe^{3+} + e^- \rightarrow Fe^{2+}$. (3) H_2O moves away from the surface. (4) Driven by the gradient of the chemical potential, Fe^{2+} and electrons migrate through the Fe_3O_4 (or FeO) layer to the Fe_2O_3 (or Fe_3O_4) core where they form additional Fe_3O_4 (or FeO) via the equation $4Fe_2O_3 + Fe^{2+} + 2e^- \rightarrow 3Fe_3O_4$ (or $Fe_3O_4 + Fe^{2+} + 2e^- \rightarrow 4FeO$).

Combing this picture with the aforementioned argument of diffusion as the rate-limiting step in the first reduction stages, it can be assumed that steps (1) or (3), corresponding to the diffusion of H_2 or H_2O (the latter process should be slower due to the larger molecular size of H_2O), or step (4), corresponding to the inward migration of Fe^{2+}, are the slowest processes in this scenario.

Considering the relatively large gas flow rate used in this work and the significantly higher coefficient of gaseous diffusion in combination with that of solid-state diffusion, it is expected that the inward transport of Fe^{2+} to the reaction interface is the rate-controlling step prior to the formation of a continuous Fe layer.

After the formation of a continuous and compact Fe layer, the further removal of oxygen from the wüstite/iron reaction interface has to take place though the iron layer, following the oxygen chemical's potential gradient. Several possible rate-determining mechanisms for this regime have been discussed in the literature [[37],[45],[49],[58],[69–71]]. According to these previous studies the FeO to Fe transition process can be divided into several kinetic steps: (1) H_2 gas molecules diffuse to the surface and (2) react with the O atoms at the external surface of the Fe layer, forming water. (3) H_2O moves away from the surface. (4) Due to a gradient in oxygen activity, O atoms diffuse through the Fe layer away from the FeO/Fe reaction front, where the FeO ↔ Fe + O equilibrium prevails, leading to (5) Fe nucleation and the steady release of O at the internal reaction front. A corresponding schematic diagram of the wüstite reduction by H_2 after the formation of a continuous Fe layer is shown in Fig. 3. As mentioned above, the specific diffusion path plays an important role during the wüstite reduction process. However, analyzing integral kinetic reduction curves is insufficient to distinguish whether the rate-determining step is the gaseous diffusion corresponding to step (1) or (3) or the outbound solid-state diffusion of oxygen corresponding to step (4).

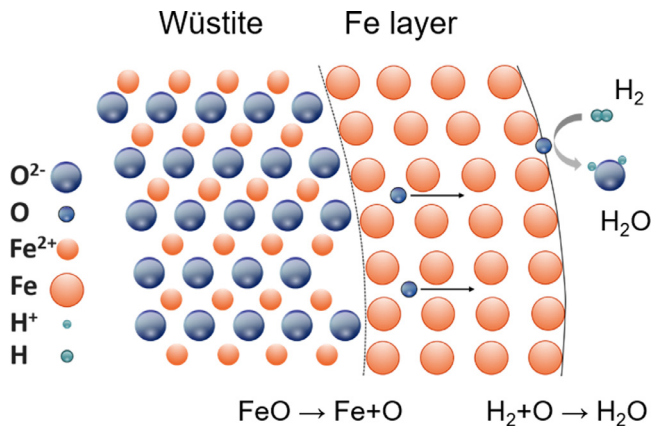

Fig. 3. Atomic-scale schematic view of the wüstite reduction by H_2 after the formation of a continuous layer of reduced Fe on the wüstite. The recombination of O and H takes place at the free surface but not at the Fe/FeO reaction interface.

Although for the $Fe_2O_3 \rightarrow Fe_3O_4$ and $Fe_3O_4 \rightarrow$ FeO transitions the respective Fe_3O_4 and FeO product layers also serve as barriers against the inward solid-state diffusion of Fe^{2+} from the surface to the reaction interface, the final Fe product layer surrounding the wüstite suppresses mass transfer much more efficiently, owing to the low diffusion coefficient particularly of O in the bcc Fe lattice [65–67]. Also, both FeO and Fe_3O_4 contain multiple defects at elevated temperatures [73]. Thus elemental diffusion through such constituents should be faster than through bulk bcc Fe when it is devoid of defects. Moreover, the reduction of Fe_2O_3 and Fe_3O_4 with hydrogen is thermodynamically more favorable than the reduction of FeO.

This first analysis and review of the existing literature shows that a more detailed interpretation of the reduction kinetics with the aim to design suited pellets and reactors for such scenarios requires information about the microstructure of the pellets, both in their initial oxidic state as well as in their partially reduced state(s). Also, more information about the distribution of the lattice defects, the pore evolution, fracture and the compactness of the iron layers is needed to interpret the reaction kinetics and develop pellets that are custom-designed for hydrogen-based reduction. Of special interest in this context are the later stages of the reaction, characterized by the reduction of the wüstite into iron. Fig. 1b and c clearly reveal that the wüstite reduction rate decreases substantially during the last 20–30% of the reduction. These findings are consistent with earlier reports stating that the hematite is reduced very rapidly, while the later stages, dominated

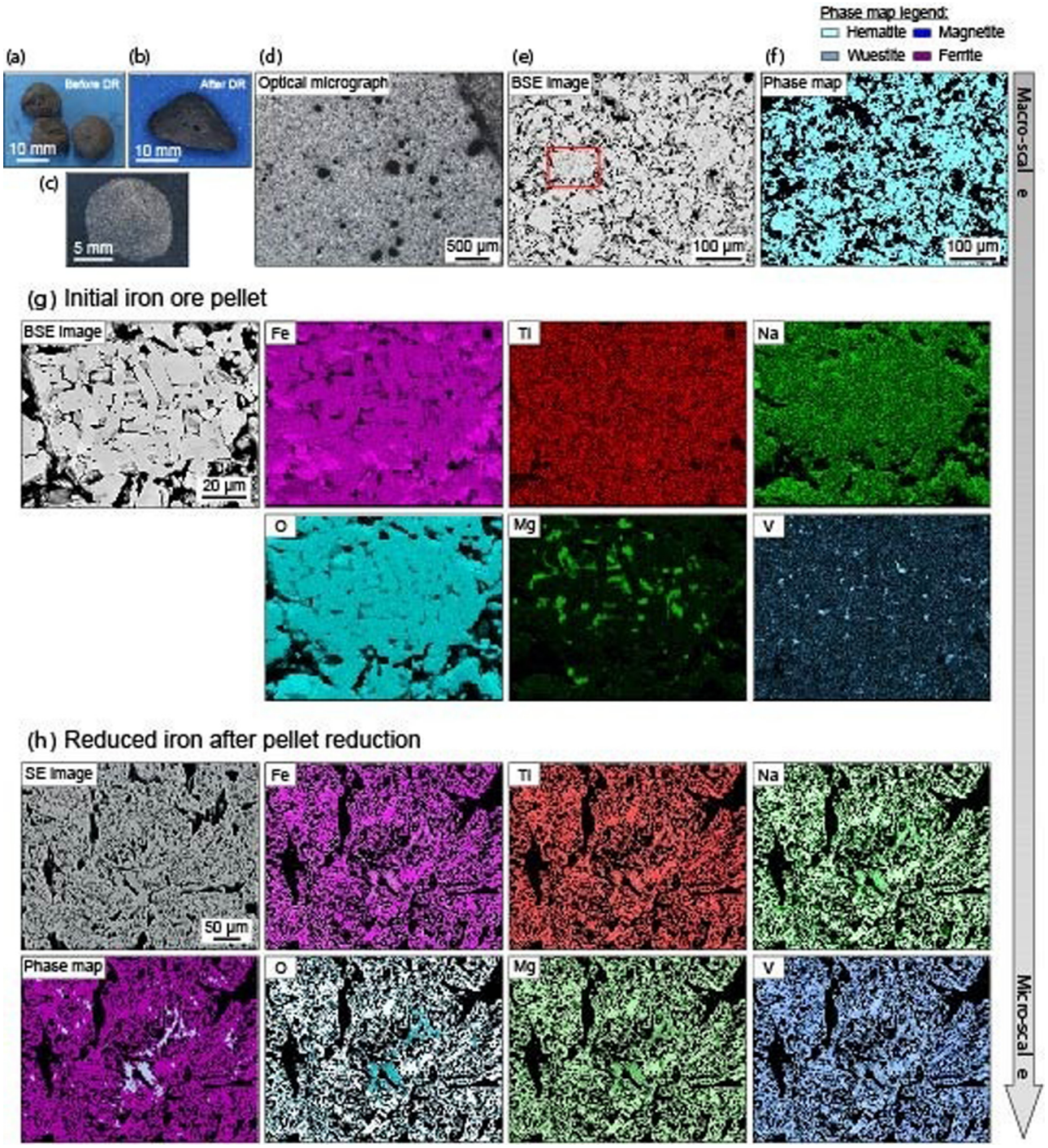

Fig. 4.. Macro- and microscale structure and chemistry characterization of dihydrogen-reduced iron ore pellets. Micrographs and EDX maps taken in the center region of the pellet. (a) Porous iron ore pellets prior to reduction. (b) Iron ore pellet after reduction by using dihydrogen. (c,d) Optical images and micrographs of the as-reduced pellet, showing porosity. (e) Backscattered electron (BSE) imaging of the unreduced pellet in the scanning electron microscope (SEM). (f) Phase map obtained from electron backscatter diffraction (EBSD). (g) BSE image and elemental maps obtained by SEM energy-dispersive X-ray spectroscopy (EDX) for the initial pellet. (h) BSE image, phase map, and elemental maps obtained by SEM energy-dispersive X-ray spectroscopy (EDX) for the H-reduced pellet (700 °C, 2 h).

by wüstite reduction, are sluggish [[74],[75]]. Microstructure observations can thus inform, which defects can enhance mass transport during this reaction stage.

4. Structure and composition analysis at macroscopic and microscopic length scales

When optically imaged, iron oxides can exhibit a variety of different colors, mainly depending on the oxidation state of the iron. Fig. 4a shows the porous iron ore pellets prior to the reduction. It has a distinct reddish color, typical for its hematite-rich composition. This color vanishes, turning black, when the iron ore is reduced to metallic iron through the reduction with hydrogen, Fig. 4b. The samples were cut and embedded (Fig. 4c) for further light (Fig. 4d) and electron optical investigation, Fig. 4e and f.

Backscattered electron (BSE) imaging of the unreduced pellet in the scanning electron microscope (SEM), Fig. 4e, reveals that the

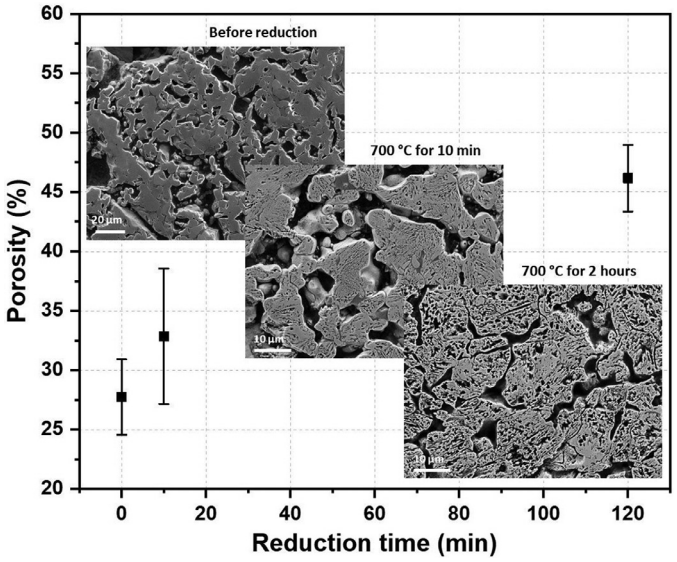

Fig. 5.. Porosity analysis as a function of the reduction time, mapped in regions at the center of the pellets. Porosity prior to reduction, measured in sets of 2D metallographic images: 27.7 ± 3.2%; 700 °C for 10 min: 32.9 ± 5.7%; 700 °C for 2 h: 46.2 ± 2.8%. Porosity analysis was conducted using the ImageJ software. For each condition, 12 SEM images were analyzed and the porosity value was averaged over 12 measurements. It should be noted that the true porosity values in 3D might deviate from these values.

microstructure consists of grains with sizes of up to tens of µm. They are separated by a fine mesh of pores, ranging from nm to multiple µm in size. The influence of the single crystal effects and grain size of the ore on reduction kinetics has been studied in the literature [[76],[77]], reporting for the case of magnetite, that the reduction kinetics gets faster with smaller grain size.

The phase map from electron backscatter diffraction (EBSD) in Fig. 4f shows that the initial ore pellet is predominantly comprised of hematite (Fe_2O_3) making up 99.3% of the volume, and a minor amount of magnetite (Fe_3O_4) of 0.7%. Elemental maps obtained by energy-dispersive X-ray spectroscopy (EDX) in the SEM are displayed in Fig. 4g for some abundant slag elements [[78],[79]], i.e. Ti, Mg, Na, V. The elemental maps highlight the compositional complexity on this scale, with a relatively homogeneous Ti distribution, while localized enrichments in Mg, Na, and V appear in intergranular regions, likely in the form of oxides, which is certainly related to the composition of the slag elements in the pellet and their solubility in hematite. The EBSD map in Fig. 4h shows that after reduction (700 °C, 2 h) 94% ferrite and 6% of retained oxide were obtained. Although the background signals are high in the EDX maps, compared with the initial ore pellet, and at that scale, all gangue elements appear to be localized in the vicinity of residual oxide clusters. It is worth noting that all the metallic slag elements in the pellet, such as Ti, Mg, Na, and V, possess a significantly higher affinity for oxygen than Fe, and hence are markedly more difficult to be reduced. The quite homogeneous appearance of the slag elements alongside with Fe on this scale is probably due to the coarse resolution. Below, we study the oxides therefore at high resolution using atom probe tomography.

Fig. 5 shows the porosity and cracks in the pellets in the initial and reduced states. While the initial sample is characterized by the pore structure inherited from pellet manufacturing (porosity of 28 vol.%), the intermediate reduction stages reveal the formation of a large number of additional lengthy and small cracks and pores in the microstructure. The reduction at 700 °C for 10 min results in an increase in the free volume by about 5% and a decrease in the average diameter of the pores from 1.70 to 0.41 μm. This strong decrease in the average diameter is due to the huge number of small pores with a size below 2 μm, Suppl. Fig. S1. After reduction at 700 °C for 2 h the porosity increases by about 13%, and the average diameter changes from 0.41 to 0.86 μm. This observation means that the microstructure of the reduced pellets does not only inherit its porosity from preceding processing, but also acquires additional free volume, together with multiple lattice defects (e.g. dislocations and cracks) due to the volume mismatch and the associated stresses between the educt and product phases.

The presence and role of porosity in iron ore pellets have been discussed in the literature. The pellets consist of iron ore fines that either arise during the processing of high-grade iron ores (i.e. > 60% Fe content), or during a beneficiation process in which most of the gangue minerals are removed from low-grade iron ores, thereby enriching their iron content. Considering the generally highly heterogeneous composition of the natural raw material combined with different processing steps that require the admixture of additives such as binders, fluxing agents, or carbon, it is not surprising that the resulting pelletized iron ores also inherit a complex pore structure across different length scales [80]. Besides this initial porosity state, it is also important to understand that the porosity changes during the course of the reduction. This is due to (a) the net volume loss as the oxygen gets removed; (b) the volume changes associated with the phase transformation sequence from hematite to wüstite and finally to iron; (c) locally trapped gas (e.g. the water) pressure aiding crack opening and (d) the micromechanical boundary conditions which create internal stresses that lead to delamination and decohesion at the hetero-interfaces [[63],[81]]. The influence of the initial porosity on reduction kinetics was studied by Weiss et al. [82], reporting also a change in porosity with progressing reduction. It was found that the degree of the acquired porosity depends on the reduction boundary conditions, particularly on temperature. Higuchi and Heerema [[83],[84]] suggested that the presence of large pores with sizes above 15 μm enhanced the reduction rate more efficiently than small pores below 15 μm. However, it must be noted that these data were acquired on a case of CO-based reduction and not for H-based reduction. This finding might be related to the relevance of capillary effects in smaller pores and cracks, as well as connectivity.

High porosity and tortuosity, i.e. the degree of the percolating topology of the internal free surface regions, provide fast diffusion pathways for the reactants and ample potential nucleation sites. The accessibility of the internal surfaces for the reduction gas substantially accelerates the global reduction kinetics. It also plays an essential role in taking up and removing the oxidation product, i.e. the water that is formed during the redox reaction.

This is also evident from Fig. 5 which reveals the significant increase in the acquired porosity and tortuosity as reduction proceeds. Noticeably, if diffusion of H_2 to or H_2O away from the pellet/gas interface was the rate-limiting step of the reaction, the reduction rate should vary with time, due to a continuously enlarged specific surface area of the pellet and the corresponding change in the gas permeability. However, the iron ore reduction exhibits a relatively stable reduction rate within the reduction degree range of ~0.33 to ~0.7 (Fig. 1b). This observation indicates that gaseous diffusion is not the key factor controlling the wüstite reduction rate but rather the internal diffusion of oxygen through the solid iron.

The tortuosity of the pores away from the pellet surface is normally quite poor, especially at the early reduction stages when pathways (e.g. cracks) to the external atmosphere have only rarely been formed. Consequently, it is necessary to understand both, the effects of the initially existing closed pores and of the gradually acquired pores on the reduction kinetics during the most sluggish step i.e. the FeO to Fe transition.

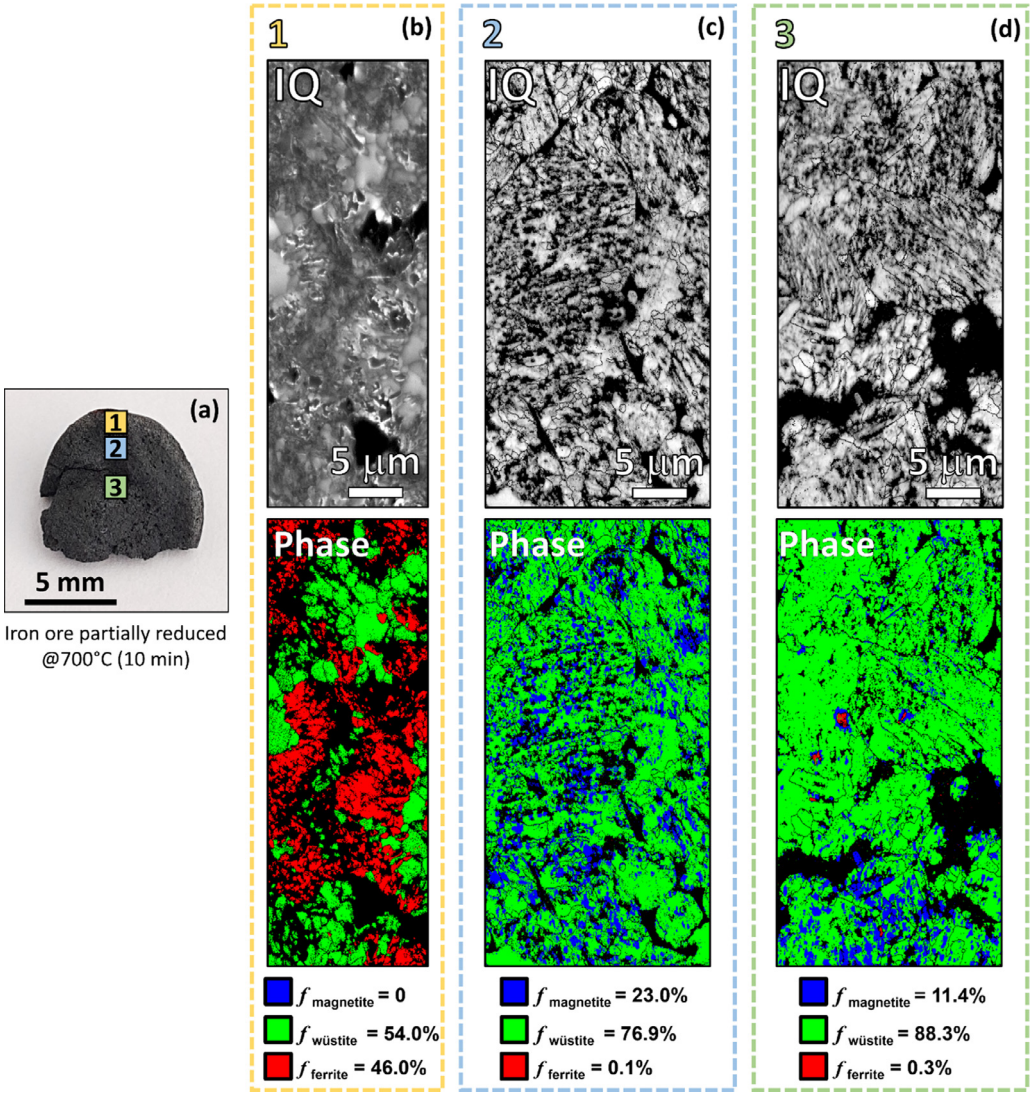

Fig. 6.. (a) Pellet phase analysis through the thickness, partially reduced at 700 °C for 10 min under an H_2 flux of 30 L/h. The yellow, blue, and green frames labeled, respectively, as 1, 2, and 3 represent the regions analyzed by means of EBSD mapping. (b) Image quality (IQ) and corresponding phase map acquired from region 1 close to the specimen's surface. (c) IQ and phase maps from region 2, found between the surface and mid-pellet. (d) IQ and phase maps from region 3 at the central position of the pellet. In all phase maps, wüstite and ferrite are represented in green and red, respectively. (For interpretation of the references to color in this figure legend, the reader is referred to the web version of this article.)

Fig. 6 reveals that strong gradients in the reduction state exist inside the pellets (10 min at 700 °C). Not many specific core-shell structure features can be observed in the individual grains (i.e. with wüstite in the center that is enclosed by a solid iron layer around it). This means that the here observed reduction process does not fully agree with the classical core-shell model [85]. The arrangement of the emerging Fe phase regions, scattered amidst the wüstite (and also partially adjacent to magnetite) implies that the description of the FeO to Fe transition stage on the basis of the shrinking core model alone can be misleading, as it does not consider the pellet's real microstructure. This observation suggests to conduct in future full-field simulations of the reduction process which are capable of considering pores, cracks and further microstructure features and the associated topo-chemical effects [86].

The images show the microstructure and the three dominant phases in different regions through the thickness of one of the pellets, as marked in Fig. 6a. The outermost region of the pellet has been reduced into nearly 50% ferrite already after 10 min. (Fig. 6b). The reaction sequence in this region and at this stage goes from wüstite to iron. The fast kinetics in this region is attributed to a shorter solid-state diffusion distance from the surface to the reaction interface and thus a faster transport of O away from the reaction interface. In the second and third set of microstructure images, taken 2 mm below the surface and in the center of the same ore particle, respectively, only less than 1 vol.% of iron has formed after 10 min of hydrogen exposure at 700 °C.

Interestingly, most of the quite few scattered Fe grains in Fig. 6c,d have not formed close to the relatively large pores which obviously are part of the initial (inherited) porosity. This could indicate that the local atmosphere in these pre-existing closed pores at this stage might have generally not been reductive enough for Fe formation, for instance, due to the presence of the oxidation product, i.e. water. This could also be indicated by the fact that many pores are accompanied or even partially surrounded by magnetite rather than by wüstite at this stage, e.g. in Fig. 6c.

At the transition stage from Fe_3O_4 to FeO, the oxygen partial pressure at the local atmosphere in the closed pores must assume a value between the FeO/Fe_3O_4 and the Fe/FeO equilibria, respectively. As the reduction progresses, the first nucleation of Fe appears, alongside the ongoing Fe_3O_4 to FeO transition, Fig. 6c. The

closed pores cannot play an important role in mass transport here, owing to a lack of sufficient connectivity. Also, the equilibrium oxygen partial pressure for Fe/FeO is significantly lower than that for FeO/Fe_3O_4, which renders the local atmosphere for the closed pores unsupportive for the preferential formation of the Fe nuclei. This means that any possible beneficial effect of the pre-existing closed pores on the reduction kinetics of the FeO to Fe transition becomes quite limited. Yet, closed pores possibly can shorten the outbound oxygen diffusion distance through short-circuit paths and serve as sink regions where water can form.

Fig. 6d also reveals the interesting detail that a few iron islands (red domains) have not only wüstite adjacent to them (which would be the expected thermodynamic reaction pathway for this temperature according to the Baur-Glaessner diagram) but they also show (at this resolution) a partial magnetite layer (blue) around them. This might have several possible reasons, such as locally deviating boundary conditions in terms of the oxygen and/or hydrogen chemical potentials, presence of water at adjacent free surfaces (cracks or nanopores), poor statistics, 3D topology effects that remain hidden when looking at the 2D maps alone, or re-oxidation of material portions that had been wüstite. However, the current probing resolution and statistics are insufficient to unequivocally explain the origin of these features. In any case, the discussion of these details underscores the necessity of understanding the role of the local chemical conditions, microstructure and pore features in that context.

Fig. 7 provides a closer view of the microstructure of the partially reduced pellet. Almost all of the Fe nuclei are present at the grain boundaries, where nucleation of new phases and fast mass transport are often favored, Fig. 7a. The microstructure images also reveal multiple delamination and crack events between ferrite and wüstite, due to the build-up of mechanical stresses associated with the transformations. More specifically, the volume shrinkage from the initial α-hematite Fe_2O_3 to the magnetite spinel Fe_3O_4 is about 1.93%. The total volume difference between hematite and wüstite is even 19%. The final mismatch between FeO and Fe is large, about 44% [87]. This creates high stresses between FeO and Fe which can be stored in the form of elastic energy, and/or released by plastic work or fracture. Particularly the elastic work can act as an obstacle against Fe nucleation. Once a Fe nucleus is formed, the large volume change and the associated deformation cannot be accommodated by elastic distortion alone but leads to the formation of cracks, creep pores, and dislocations. This is revealed by the microstructure presented in Fig. 7: the secondary electron image shows a variety of pores, cracks, and delamination features of different size and morphology. Fig. 7c shows several such delamination effects between the ferrite and the adjacent wüstite. Local cracking and delamination provides new free volume in the system and thus contributes to locally enhanced kinetics of the wüstite reduction, as it enables faster diffusion.

Fig. 7d-g show that the volume mismatch and the associated high-temperature deformation of the two adjacent phases lead to the substantial accumulation of dislocations, as revealed in Fig. 7e through electron channeling contrast imaging (ECCI). The associated curvature of the lattice close to the interfaces is revealed in Fig. 7f and g in terms of the gradual crystallographic rotation near some of the hetero-interfaces, a feature which translates to arrays of geometrically necessary dislocations. Transport of H (inbound) [67] and O (outbound) [[65],[66]] through these crystal defects might play a vital role in the kinetics (particularly the removal of oxygen), especially during the later stage of wüstite reduction when a relatively thick reduced iron layer surrounds the remaining wüstite islands in an approximate core-shell type morphology.

The data and the discussion so far clearly show that the microstructure plays an important role in the hydrogen-based reduction kinetics of iron ore pellets. The microstructure of the pellets consists of multiple pores (both, isolated and interconnected ones), heterophase-interfaces, grain boundaries, dislocations and cracks which can all become relevant for specific aspects of transport, reactivity, reactant recombination and water trapping. When aiming at the design of pellets and process conditions that are particularly suited for hydrogen-based reduction and specific reactor types, it is helpful to differentiate between those microstructure features that are inherited from pellet manufacturing and those that evolve during the reduction, due to mass loss, non-volume conserving transformations and mechanical stresses that lead to decohesion and internal damage.

For this reason, we conducted experiments on single crystalline wüstite specimens with (100) orientation, which were devoid of any inherited microstructure features prior to hydrogen reduction. We subjected this single crystalline laboratory-grown FeO model material to the same reduction conditions as the pellets. The SEM and EBSD investigations show that this originally fully compact and dense single crystal evolves into a highly porous and modestly polycrystalline iron compound after 2 h hydrogen-based reduction at 700 °C, Fig. 8. The high porosity range of about 30–45 vol.% (depending on probing position) is similar to the expected value of about 42 vol.% volume loss which occurs when reducing $Fe_{0.95}O$ wüstite to pure bcc iron.

The microstructure and crystallographic texture measurements, represented here in terms of SEM images (Fig. 8a,b) and two EBSD maps (Fig. 8c,d), taken at the center and surface regions of the hydrogen-reduced wüstite single crystal, show the formation of a massive population of pores. The newly formed iron has a very strong crystallographic texture, which indicates an oriented nucleation mechanism by which the iron forms on the wüstite.

These results about the acquired porosity confirm that the global kinetics of the hydrogen-based reduction of iron oxide cannot be solely interpreted in terms of the classical core-shell model.

5. Structure and composition analysis at near-atomic scale

Some studies on H-based hematite reduction have discussed the role of the oxide gangue [[88],[89]], however, no chemical analysis at high spatial resolution has been conducted so far, and reports on the global chemical composition of ores do not provide a consistent picture of the effects of chemical impurities on the reduction kinetics and on the associated mechanisms.

Elemental inhomogeneity is not only a feature visible at the macro- and/or micro-scale, such as shown in Fig. 4, but can also be observed at the reaction front at the atomic scale. For revealing the possible role of non-ferrous oxides on the reduction kinetics at the reaction front, we studied the distribution of impurities by atom probe tomography (APT), before and after complete reduction. Details on the experimental protocols are given in the supplemental Fig. S2–S5.

The three-dimensional atom maps obtained from the as-received hematite ore are shown in Fig. 9a, in which Fe atoms are shown in pink and O atoms in cyan. The data set has an average Fe and O content of 44.4 and 51.6 at.%, respectively, translating to a stoichiometry ratio of 0.86 (see Table S2 for atomic composition details) although the expected stoichiometric ratio of hematite is 0.67. The O depletion in the composition can be explained by the loss of neutral O during field evaporation as desorbed neutral O atoms and also O_2 molecules do not contribute to the detector signal [[36],[90],[91]]. Fig. S6 shows a multiple-event correlation histogram that reveals significant tracks indicative for the formation of neutral oxygen species through the decomposition of $FeO_2^+ \rightarrow Fe^+ + O_2$ and $FeO_3^+ \rightarrow FeO^+ + O_2$ during the APT measurement.

The most abundant gangue elements such as Mg, Al, Ti, and V exhibit a homogeneous distribution in the initial iron ore on the

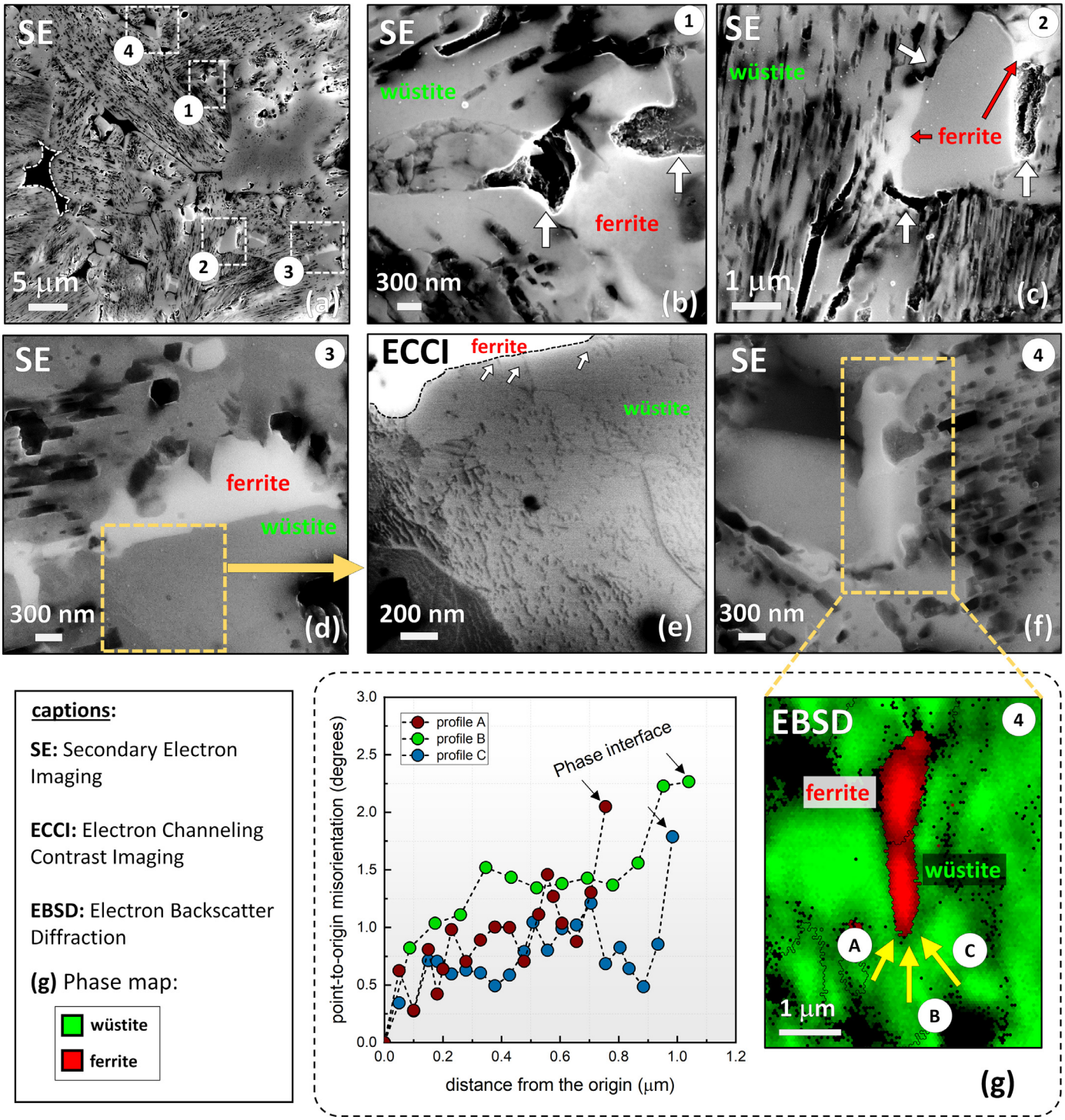

Fig. 7.. Correlative SE and ECCI analysis for region 2 (about 2 mm below the pellet surface) of the partially reduced pellet (10 min, 700°C) shown in Fig. 5. (a) SE image of the map of the pellet microstructure. The white frames marked as 1, 2, and 3 highlight specific regions whose enlarged views are given in (b), (c), and (d), respectively. (e) ECCI image obtained from the area delimited by the yellow frame in (d). (f) SE image from the area labeled as 4 in (a). The arrows A, B, and C were used as a reference to obtain local orientation gradients. (g) EBSD phase map from the area delimited by the yellow frame shown in (f). Point-to-origin local misorientation profiles acquired along the arrows A, B, and C in (f). (For interpretation of the references to color in this figure legend, the reader is referred to the web version of this article.)

nano-scale, as revealed by a nearest-neighbor analysis presented in Fig. S8. Fig. 9b shows a reconstructed 3D atom map of the reduced iron ore exhibiting a Fe content of 98.6 at.%, with a residual oxygen content of 0.01 at.%. Retained crystallographic information from the APT data confirms the body-centered cubic crystal structure (Fig. S9). Major impurity elements such as Mg, Al, and Ti are not detected within reduced α-Fe but trace amounts of V at 100 ppm level are observed (see Table S2).

Another dataset displayed in Fig. 9 contains a nano-sized oxygen-rich platelet embedded within the reduced α-Fe matrix, which appears to be crystallographically aligned along the {002} planes of the bcc structure (details in Fig. S10). The composition of the remaining, trapped oxide is complex: it contains 33.3 at.% O

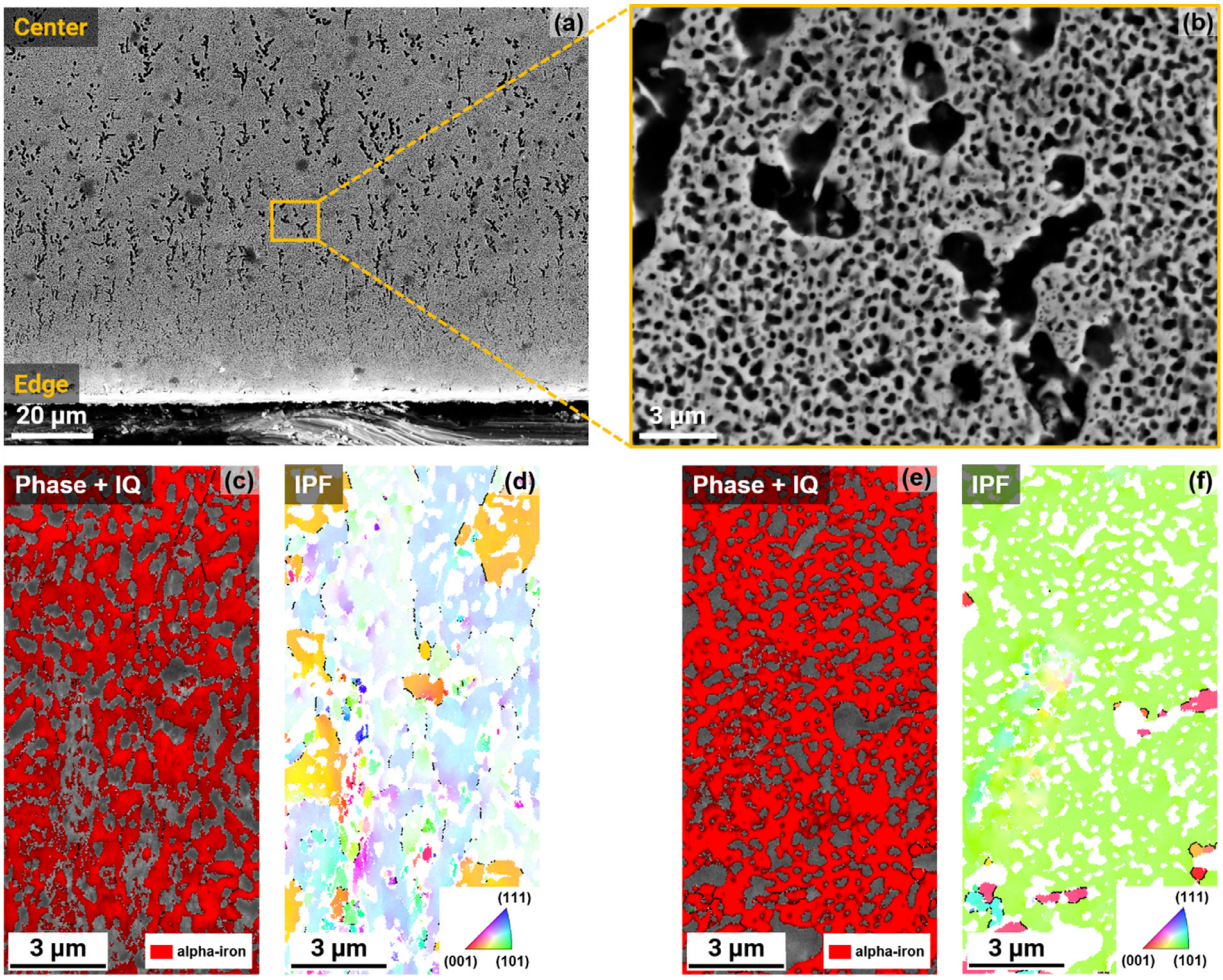

Fig. 8.. SEM and EBSD mapping on a hydrogen-reduced single crystalline FeO specimen (a,b). The original wüstite (100) crystal was compact and devoid of defects or pores. EBSD phase map overlaid on image quality (IQ) map from the (c) surface and (e) center region of the hydrogen-reduced wüstite single crystal; (d) and (f) corresponding inverse pole figure (IPF) maps of the crystallographic textures of the phase maps shown in (c) and (e). The analysis shows the formation of a massive population of pores during the reduction process of the originally fully compact wüstite single crystal. The crystallographic texture of the newly formed iron shows a texture inheritance effect, indicating an oriented nucleation mechanism of the iron on the wüstite.

and the rest consists of several metals, namely, 36.7 at% Fe and 19.1 at% V, as well as low amounts, below 3 at%, of the other gangue elements Mg, Al, and Ti, as revealed by the one-dimensional composition profile in Fig. 9d. The nano-sized oxygen islands remaining also after reduction, originate from the gangue oxides and not from Fe-based oxide as they have low oxide-formation free energies at the reduction conditions according to Ellingham's diagram [92].

During the reduction process, oxidized species of less noble elements such as Al, Mg, and Na cannot be reduced. When they are relatively homogeneously distributed inside the iron oxide, they can either remain in the form of tiny oxide nano-particles, which might be thermodynamically not favorable (as the interface energy between oxide and metal is generally high), or they can be expelled from the reduction front into the remaining oxide. As the size of the remaining oxide shrinks, this oxide will become enriched by these species, and the highest concentration of the slowest diffusing and strongest bonded elements will accumulate at the interfaces. The enrichment of the less noble elements at the interface might significantly influence the further reduction.

The APT results also show that several gangue-related impurities indeed get captured in nano-sized metastable oxides, possibly on the way to the spinel phase formation. The observed ratio of O to metal ions is unlike any of those reported for typical Fe-rich oxides, including those in the Fe-V-O system [93]. A Fe_2O oxide mineral was reported to be stable at high pressures such as those encountered in the Earth's core [[94],[95]] and off-stoichiometric amorphous Fe-rich oxides with similar compositions have been reported in tribological layers [96]. Here, while embedded within the metallic lattice and in the harsh conditions of the reduction (i.e. 30 L/h of H_2 gas flow at 700 °C), out-of-equilibrium, transient states are likely to appear.

Some details of the composition of these remaining oxide particles are worth to be further explored. It is conceivable that the harsh reaction conditions have enabled diffusion of these elements out of the $Fe(O_x)$ matrix, resulting in chemical partitioning across the metal/oxide interfaces and within the remaining oxide. The Na appears segregated at the interface. As the mobility of Na is comparatively poor due to its large ionic radius, Na is supposed to be one of the last gangue elements reaching the nano-sized oxides. The solubility of Na in the residual oxides is also expected to be low on account of the large difference in the ionic radii, which, accompanied by the belated arrival of Na, leads to its enrichment at the metal/oxide interface. From the tomogram of the oxide, most Na atoms (in green) are segregated at the apex of the oxide platelet, possibly a region of higher tensile stress where the large Na ions would be better accommodated.

Fig. 10 reveals that at the later reduction stage FeO might be reduced to Fe via transient states due to the influence of certain

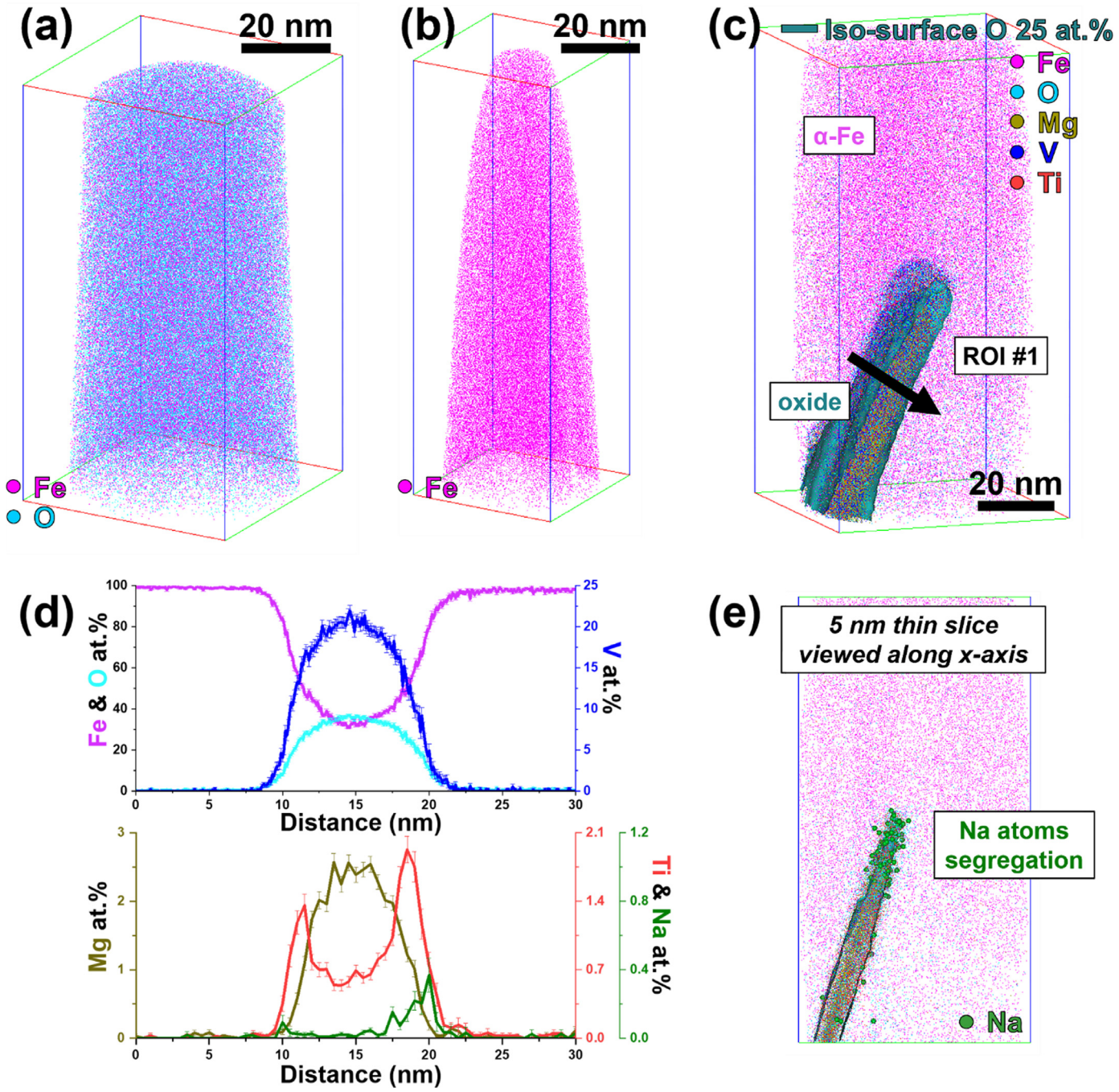

Fig. 9.. 3D atom maps of (a) before and (b) after the direct reduction of as-received hematite ore, from a region about 1 mm below the pellet surface. Pink and cyan dots in the 3D reconstructions represent individual Fe and O atoms, respectively. (c) A reconstructed 3D atom map acquired from as-reduced ore. Iso-surface of O at 25 at.% (cyan) represents the interface between α-Fe and the wüstite oxide. The inset is a 3D atom map of a 5 nm thin slice. (d) Corresponding one-dimensional composition profile from the cylindrical region of interest, marked as ROI #1, (Ø15 $\times$ 30 nm^3) across the oxide nano-feature. (e) Na segregation at the interface between the retained oxide and the reduced matrix. Pink, cyan, golden brown, red, blue, and green dots represent the reconstructed positions of Fe, O, Mg, Ti, V, and Na atoms, respectively.

gangue elements. Actually, this process can start much earlier than expected, as can be seen in Fig. S11 of an impurity-doped oxide with a Fe to O ratio of 3.3 just after 30 min reduction. A deeper reduction of the nano-sized residual oxide should lead to the formation of a remaining Fe-depleted oxide, as clearly illustrated in Fig. 10, where phase separation between Fe-rich and Fe-depleted oxides appears. Ti and Mg are enriched in different oxides, as revealed in Fig. 10a. Here the Fe to O ratio in the Fe-rich oxide is remarkably lower than that of its counterpart in Fig. 9 (Table S2), which further indicates a higher reduction degree for the two-phase oxide.

Fig. 10b shows a series of slices through the tomogram evidencing the separation between the two oxide variants. Fig. 10c is a composition profile evidencing that Mg partitions to the Fe-rich oxide and Ti in the Fe-depleted oxide, while Na is segregated at the interface between the two oxides.

The Fe-rich oxide is mainly composed of V and Fe, with the V to Fe ratio remaining at a rather constant value slightly above 2 along the distance, which can be best ascribed to Mg-doped FeV_2O_4 (also

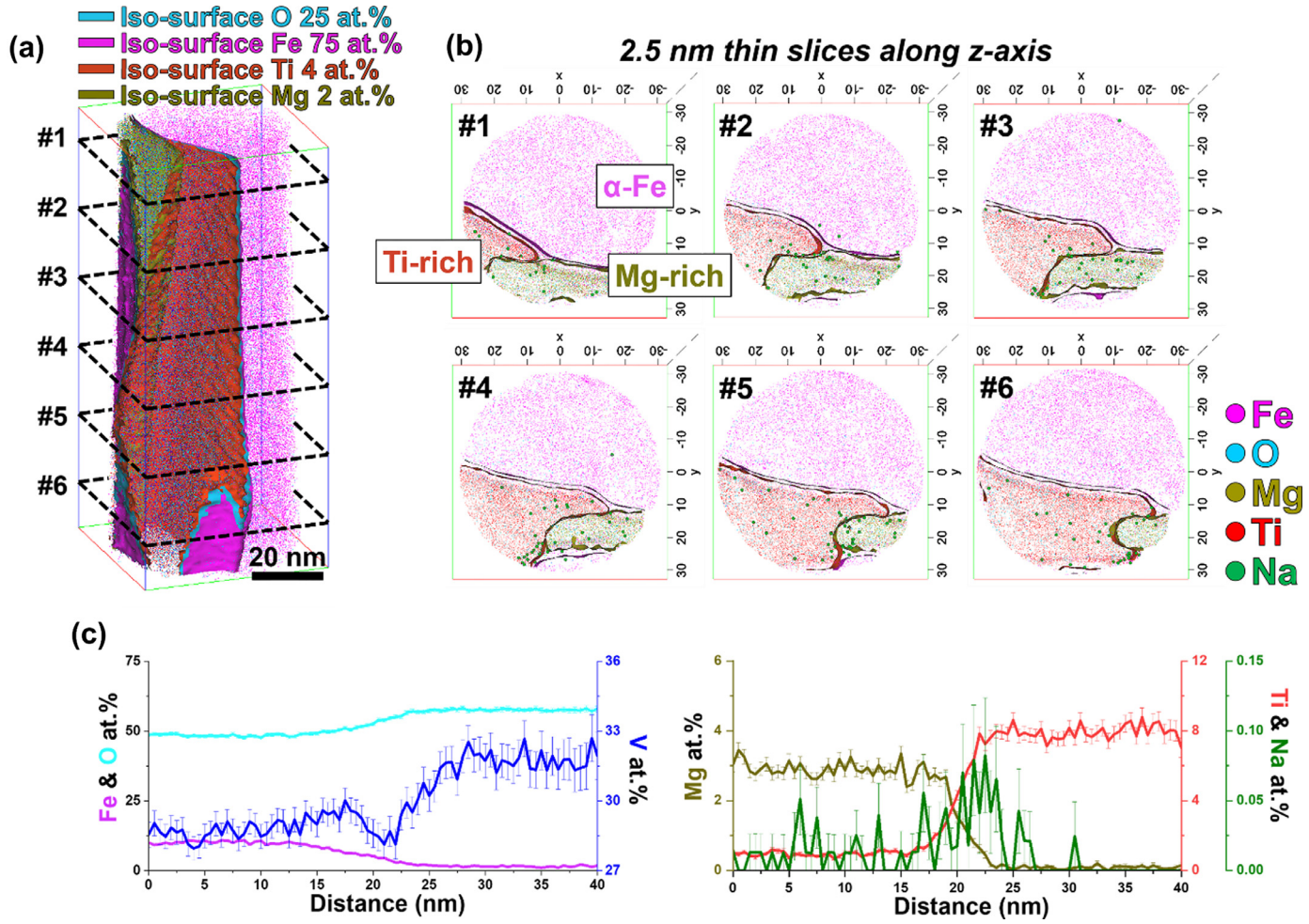

Fig. 10.. Atom probe tomography analysis of partially reduced iron oxide, from a region about 1 mm below the pellet surface. (a) 3D atom map showing the distribution of selected major species with Mg- and Ti-rich oxides phases highlighted in 2 and 4 at.% iso-surfaces, respectively. (b) series of 2.5nm-thick slices through the reconstructed point cloud. (c) one-dimensional composition profiles (Ø7.5 × 40 nm^3) across the adjacent oxides. (For interpretation of the references to color in this figure legend, the reader is referred to the web version of this article.)

doped with other gangue elements, as documented in more detail in Table S2). The Fe-depleted oxide is mainly consisting of V and Ti, probably corresponding to $(V,Ti)_2O_3$, as the metal to O ratio of the Fe-depleted oxide (0.83) is quite similar to the Fe to O ratio of Fe_2O_3 (0.86) acquired by APT. Also, the solubility of Ti in V_2O_3 is relatively high. The identification of the two-phase oxide is reasonable also from a thermodynamic perspective, as the thermodynamic onset of the oxygen partial pressure follows the sequence: V_2O_3<FeV_2O_4<FeO.

To study the role of Na that was observed at several hetero-interfaces between mixed oxides and iron (Figs. 9e, 10c) in a specimen without an inherited microstructure, atom probe tomography experiments were conducted also on a wüstite single crystal, Figs. 8, 11. The data show representative results before (Fig. 11a) and after partial (Fig. 11b) wüstite H-reduction. Two observations are of specific interest here. First, solute Na is enriched at the hetero-interface (Fig. 11b) and second, the oxygen content of the wüstite close to the iron interface is depleted to oxygen values below the expected equilibrium stoichiometry $Fe_{(1-x)}O$, with X varying at 700 °C between about 0.90 and to 0.97 [32–37].

The first observation matches the findings from the other samples, namely, that Na segregates at the hetero-interfaces between oxides and iron, an effect which might influence the kinetics of the transformation and the motion of the reaction front. The second point, i.e. the under-stoichiometric oxygen content of the wüstite adjacent to reduced iron must be seen in light of two effects. The first effect is due to possible experimental errors, related to the recombination of oxygen ions at the atom probe tip surface into neutral species, depending on local electrical field strength [[91],[97]]. This effect might lead to the apparent loss of oxygen as the spectrometry only counts charged particles. Clarification of the magnitude of this effect requires for the specific case of wüstite reduction more detailed instrumental follow-up experiments. The second reason for the low oxygen content can be seen in the interplay of the elementary diffusion steps during the progressing reduction across the hetero-interface [[57],[98]]. The chemical potential of the oxygen forms a steep gradient into the freshly reduced iron. The actual concentration profiles for Fe and O across the interface are then determined by their respective diffusion rates.

Regarding the tramp elements in the ores it needs to be emphasized that no matter which kind of Fe-containing oxide of gangue elements is formed during the wüstite reduction process, the equilibrium oxygen partial pressure for Fe/transient-state oxide must be at a value below that for Fe/FeO (e.g., the thermodynamic onset of FeV_2O_4 formation is three orders of magnitude lower than that for FeO at 700 °C). This means that the oxygen gradient from the reaction interface to the surface will be lowered due to the formation of the transient-state oxide (when assuming the same thickness) and thus the diffusion of O through the Fe product layer will be further reduced. The formation of the Fe-containing intermedi-

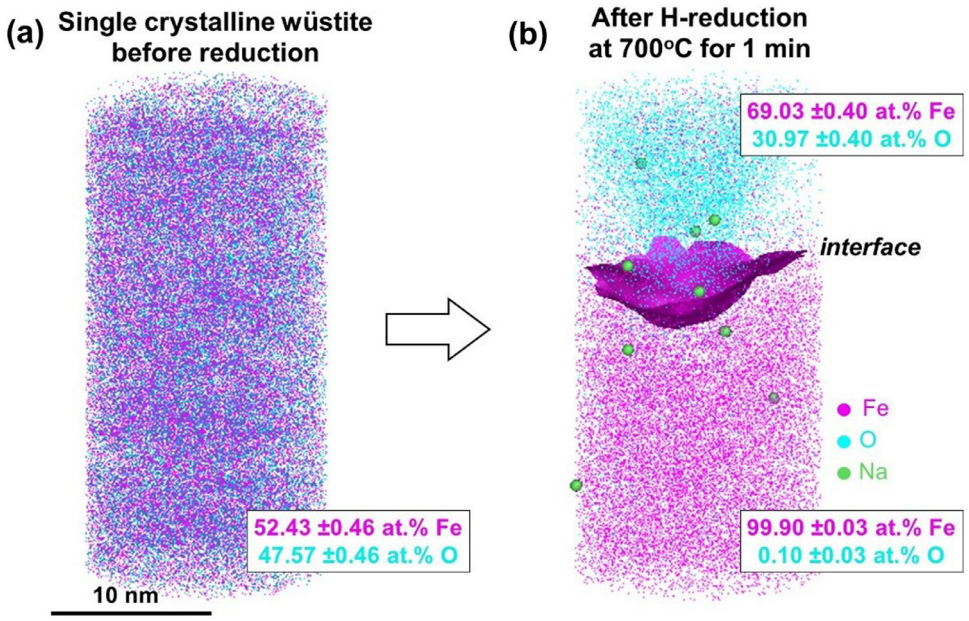

Fig. 11.. Atom probe tomography analysis of single crystalline wüstite before (a) and after (b) H-based reduction. (b) Interface region between iron and wüstite with minor Na segregation. The iso-composition surface shown in purple marks 75 at.% Fe.

ate oxide plays a critical role in the significantly reduced kinetics during the final 20% reduction regime.

Understanding the behavior of gangue-related tramp elements allows us to identify kinetically relevant factors with respect to beneficial (catalysis effects) or harmful (delayed reaction rate) influence on the reduction reaction. Typical gangue compounds observed in direct reduction pellets are mostly Si-, Al-, Mg-, Na- and Ca- containing oxides. While reports by Wang and Sohn [[99],[100]] indicated that Ca- and Si oxides may alter the volume changes during reduction and affect the reduction rate, other papers found no clear trend of the influence of these oxides on the kinetics [[27],[60]]. Depending on the content and conditions, MgO was reported to either lower the reducibility of sintered hematite [101] or promoting its reduction [[88],[102]]. Al_2O_3 was observed to affect the reduction rate of magnetite as it triggers the formation of a network-like wüstite structure. The highest reduction rate was observed when adding 3 wt.% Al_2O_3 into the magnetite [103]. A TiO_2 content $>$ 0.5 wt.% was reported to significantly increase the reduction induced degradation, resulting in heavily cracked pellets [104]. The thickness of the formed Fe crystals gradually increases with increasing V_2O_5 additions in magnetite, which facilitates the aggregation and diffusion of Fe atoms [105].

Inconsistencies in some of these trends can now be better understood in terms of the fact that these studies were performed on the macro- and/or micro-scale and not at the near-atomic-scale at which the actual rate-limiting processes take place. Furthermore, revealing the effect of the gangue elements on the most sluggish step, i.e. the wüstite reduction, should be more beneficial for an in-depth understanding of the reduction kinetics, which, however, is rarely reported. Our APT results indicate that among the many gangue elements, special attention should be placed on those that can form mixed oxides with Fe and those that can be enriched at the Fe/oxide interface at the wüstite reduction stage.

The effects of the nano-scale chemistry on the reduction must be assessed further, as indeed most of the oxides encountered here play a critical role in the reduction process itself. There are many unknowns in the atomic-scale processes of how the local composition of the material affects the solid-state diffusion of elements, especially O and how the gangue elements accumulated at the metal/oxide interface influence the reduction kinetics. Of high relevance is also the effect of certain gangue elements on the formation of the transient-state oxide during the FeO to Fe transition and the interplay between the transient-state oxide and iron phases.

6. Conclusions and outlook

The impact of steel production via the conventional blast furnace and converter route, using carbon as a reductant, on the greenhouse gas emission is staggering, causing about 6.5% of all global CO_2 emissions. Reducing iron ores with hydrogen, via the solid-state direct reduction route, offers a viable alternative. The main challenge to solve, however, is to understand the origin of the sluggish reduction kinetics, particularly during the later stages of the wüstite-to-iron reduction.

Here, we conducted a study about the role of the micro- and nanostructure of the ores, both inherited and acquired during reduction, and about the nano-chemistry.

We find that the relatively easy nucleation of magnetite and the subsequent wüstite as well as the fast solid-state diffusion (most likely inward diffusion of Fe^{2+}) through the iron oxide product layer are the main reasons for the fast reduction kinetics of the hematite to wüstite. The third step, viz. the reduction of wüstite into iron is – during the final 20% reduction regime – nearly an order of magnitude slower. This effect can be most likely attributed to the sluggish mass transport (particularly of the outbound O solid-state diffusion) through the already formed iron product layers surrounding the wüstite.

The role of the pre-existing closed pores in the kinetics of the wüstite reduction is quite limited in view of the high nucleation barrier for Fe to form. Fe nuclei tend to preferentially form at the wüstite grain boundaries rather than at pores. This observation suggests that the pores are mostly closed rather than interconnected. The fast reduction at the external regions of the pellets is thus due to the short diffusion distances of O from the reaction interface to the surface. This supports the general observation that the outbound diffusion of O plays the dominant important role in the reduction kinetics.

The high volume mismatch between the wüstite and Fe leads to delamination cracks and high dislocation densities which might

locally aid mass transport and thus the reduction process. This effect is, however, less relevant to notably mitigate the overall kinetic deceleration observed towards the later reduction stages.

Near-atomic scale chemical probing reveals the presence of nano-sized Fe-containing transient-state oxides and the accumulation of certain gangue elements i.e. Ti and Na at the metal/oxide interface, both of which are assumed to be another cause for the slow reduction kinetics at the late stages of the wüstite reduction.

Approaches to enhance reduction kinetics are, therefore, a high degree of plastic deformation and micro-cracking of the ore pellets (before and during reduction), providing more percolating free volume for accelerated mass transport; elimination of certain stable oxide-forming tramp elements stemming from the gangue; elimination of certain gangue elements that form ions with large radii; and smaller pellets containing small randomly oriented grains. A way towards enhanced reaction kinetics for instance in fluidized-bed direct reduction furnaces might thus also lead through a somewhat counterintuitive approach, namely, to make the pellets mechanically weaker (rather than stronger) so that they break in the reactor under well-defined loads during the wüstite reduction step, yet, without leading to undesired sticking.

Declaration of Competing Interest

None

Acknowledgements

We thank Uwe Tezins, Christian Broß, and Andreas Sturm for their support to the FIB & APT facilities at MPIE. We are grateful for the financial support from the BMBF via the project UGSLIT and the Max-Planck Gesellschaft via the Laplace project. BG and SHK acknowledge financial support from the ERC–CoG-SHINE-771602. KS is grateful to the IMPRS-SURMAT for funding of his scholarship.

Supplementary materials

Supplementary material associated with this article can be found, in the online version, at doi:10.1016/j.actamat.2021.116933.

References

[1] M. Ashby, Materials and the environment: eco-informed material choice: second edition, 2012. https://doi.org/ 10.1016/C2010-0-66554-0.
[2] A.C.H. Allwood, J.M. Cullen, J.M. Carruth, M.A. Cooper, D.R. McBrien, M. Milford, R.L. Moynihan, M.C. Patel, S. Bauer, Sustainable Materials: With Both Eyes Open, UIT Cambridge Ltd, Cambridge, England, 2012, doi:10.1016/s1369-7021(12)70169-4.
[3] T.E. Graedel, J. Allwood, J.P. Birat, M. Buchert, C. Hagelüken, B.K. Reck, S.F. Sibley, G. Sonnemann, What do we know about metal recycling rates? J. Ind. Ecol. 15 (2011) 355–366, doi:10.1111/j.1530-9290.2011.00342.x.
[4] D. Raabe, C.C. Tasan, E.A. Olivetti, Strategies For Improving the Sustainability of Structural Metals, Springer US, 2019, doi:10.1038/s41586-019-1702-5.
[5] E. Basson, Major steel-producing countries 2018 and 2019 million, 2020 World Steel Fig. (2020) 1–8. https://www.worldsteel.org/publications/fact-sheets.html.
[6] J.P. Birat, F. Hanrot, G. Danloy, CO_2 Mitigation Technologies in the Steel industry: A benchmarking Study Based On Process Calculations, Stahl Und Eisen 123 (9) (2003) 69–72.
[7] D. Gielen, CO_2 removal in the iron and steel industry, Energy Convers Manag. 44 (2003) 1027–1037, doi:10.1016/S0196-8904(02)00111-5.
[8] J.M. Allwood, J.M. Cullen, R.L. Milford, Options for achieving a 50% cut in industrial carbon emissions by 2050, Environ. Sci. Technol. 44 (2010) 1888–1894, doi:10.1021/es902909k.
[9] H.H. Khoo, R.B.H. Tan, Life cycle investigation of CO_2 recovery and sequestration, Environ. Sci. Technol. 40 (2006) 4016–4024, doi:10.1021/es051882a.
[10] H.H. Khoo, J. Bu, R.L. Wong, S.Y. Kuan, P.N. Sharratt, Carbon capture and utilization: preliminary life cycle CO_2, energy, and cost results of potential mineral carbonation, Energy Procedia (2011) 2494–2501, doi:10.1016/j.egypro.2011.02.145.
[11] M. Celia, S. Bachu, Geological sequestration of CO_2 is leakage unavoidable and acceptable? in: Proceedings of the Greenh. Gas Control Technologies - 6th International Conference, 2003, pp. 477–482, doi:10.1016/b978-008044276-1/50076-3.
[12] H. Ohno, K. Matsubae, K. Nakajima, Y. Kondo, S. Nakamura, T. Nagasaka, Toward the efficient recycling of alloying elements from end of life vehicle steel scrap, Resour. Conserv. Recycl. 100 (2015) 11–20, doi:10.1016/j.resconrec.2015.04.001.
[13] B. Yuan, O.E. Kongstein, G.M. Haarberg, Electrowinning of iron in aqueous alkaline solution using a rotating cathode, J. Electrochem. Soc. 156 (2009) D64, doi:10.1149/1.3039998.
[14] B. Yuan, G.M. Haarberg, Electrodeposition of iron in aqueous alkaline solution: an alternative to carbothermic reduction, ECS Trans. 16 (2019) 31–37, doi:10.1149/1.3114006.
[15] G.M. Haarberg, B. Khalaghi, Electrodeoxidation of Iron oxide in aqueous NaOH electrolyte, 2020 MA2020-011275–1275https://doi.org/, doi:10.1149/ma2020-01211275mtgabs.
[16] D. Spreitzer, J. Schenk, Reduction of iron oxides with hydrogen-a review, Steel Res. Int. 90 (2019) 1900108, doi:10.1002/srin.201900108.
[17] K. Nishihiro, T. Maeda, K. ichiro Ohno, K. Kunitomo, Effect of H_2 concentration on carbon deposition reaction by CO–H_2 gas mixture at 773K to 973K, ISIJ Int. 59 (2019) 634–642, doi:10.2355/isijinternational.ISIJINT-2018-393.
[18] K. Nishihiro, T. Maeda, K. ichiro Ohno, K. Kunitomo, Effect of temperature and CO_2 concentration on gasification behavior of carbon fiber containing fine iron particles, ISIJ Int. 59 (2019) 2142–2148, doi:10.2355/isijinternational.ISIJINT-2019-240.
[19] H. Nogami, Y. Kashiwaya, D. Yamada, Simulation of blast furnace operation with intensive hydrogen injection, ISIJ Int. 52 (2012) 1523–1527, doi:10.2355/isijinternational.52.1523.
[20] A.J. Fortini, D.D. Perlmutter, Porosity effects in hydrogen reduction of iron oxides, AIChE J. 35 (1989) 1245–1252, doi:10.1002/aic.690350803.
[21] M. Fischedick, J. Marzinkowski, P. Winzer, M. Weigel, Techno-economic evaluation of innovative steel production technologies, J. Clean. Prod. 84 (2014) 563–580, doi:10.1016/j.jclepro.2014.05.063.
[22] M. Weigel, M. Fischedick, J. Marzinkowski, P. Winzer, Multicriteria analysis of primary steelmaking technologies, J. Clean. Prod. 112 (2016) 1064–1076, doi:10.1016/j.jclepro.2015.07.132.
[23] W.H. Chen, M.R. Lin, T.S. Leu, S.W. Du, An evaluation of hydrogen production from the perspective of using blast furnace gas and coke oven gas as feedstocks, Int. J. Hydrog. Energy. 36 (2011) 11727–11737, doi:10.1016/j.ijhydene.2011.06.049.
[24] W.H. Chen, M.R. Lin, A.B. Yu, S.W. Du, T.S. Leu, Hydrogen production from steam reforming of coke oven gas and its utility for indirect reduction of iron oxides in blast furnace, Int. J. Hydrog. Energy. 37 (2012) 11748–11758, doi:10.1016/j.ijhydene.2012.05.021.
[25] N.G. Gallegos, M.A. Apecetche, Kinetic study of haematite reduction by hydrogen, J. Mater. Sci. 23 (1988) 451–458, doi:10.1007/BF01174669.
[26] A. Bonalde, A. Henriquez, M. Manrique, Kinetic analysis of the iron oxide reduction using hydrogen-carbon monoxide mixtures as reducing agent, ISIJ Int. 45 (2005) 1255–1260, doi:10.2355/isijinternational.45.1255.
[27] E.T. Turkdogan, J.V. Vinters, Gaseous reduction of iron oxides: part I. Reduction of hematite in hydrogen, Metall. Mater. Trans. B 2 (1971) 3175–3188, doi:10.1007/bf02814970.
[28] M.V.C. Sastri, R.P. Viswanath, B. Viswanathan, Studies on the reduction of iron oxide with hydrogen, Int. J. Hydrog. Energy 7 (1982) 951–955, doi:10.1016/0360-3199(82)90163-X.
[29] H.Y. Lin, Y.W. Chen, C. Li, The mechanism of reduction of iron oxide by hydrogen, Thermochim. Acta 400 (2003) 61–67, doi:10.1016/S0040-6031(02)00478-1.
[30] M. Moukassi, P. Steinmetz, B. Dupre, C. Gleitzer, A study of the mechanism of reduction with hydrogen of pure wustite single crystals, Metall. Trans. B 14 (1983) 125–132, doi:10.1007/BF02670879.
[31] A. Khawam, D.R. Flanagan, Solid-state kinetic models: basics and mathematical fundamentals, J. Phys. Chem. B 110 (2006) 17315–17328, doi:10.1021/jp062746a.
[32] J.R. Gavarri, C. Carel, The complex nonstoichiometry of wüstite $Fe_{1-z}O$: review and comments, Prog. Solid State Chem. 53 (2019) 27–49, doi:10.1016/j.progsolidstchem.2018.10.001.
[33] J. Berthon, A. Revcolevschi, H. Morikawa, B. Touzelin, Growth of wustite ($Fe_{1-x}O$) crystals of various stoichiometries, J. Cryst. Growth 47 (1979) 736–738, doi:10.1016/0022-0248(79)90020-4.
[34] T. Hidayat, D. Shishin, E. Jak, S.A. Decterov, Thermodynamic reevaluation of the Fe-O system, Calphad 48 (2015) 131–144, doi:10.1016/j.calphad.2014.12.005.
[35] G.S. Parkinson, Iron oxide surfaces, Surf. Sci. Rep. 71 (2016) 272–365, doi:10.1016/j.surfrep.2016.02.001.
[36] M. Bachhav, R. Danoix, F. Danoix, B. Hannoyer, S. Ogale, F. Vurpillot, Investigation of wustite ($Fe_{1-x}O$) by femtosecond laser assisted atom probe tomography, Ultramicroscopy 111 (2011) 584–588, doi:10.1016/j.ultramic.2010.11.023.
[37] J. Zieliński, I. Zglinicka, L. Znak, Z. Kaszkur, Reduction of Fe_2O_3 with hydrogen, Appl. Catal. A Gen. 381 (2010) 191–196, doi:10.1016/j.apcata.2010.04.003.
[38] M.J. Tiernan, P.A. Barnes, G.M.B. Parkes, Reduction of iron oxide catalysts: the investigation of kinetic parameters using rate perturbation and linear heating thermoanalytical techniques, J. Phys. Chem. B 105 (2001) 220–228, doi:10.1021/jp003189.
[39] A. Pineau, N. Kanari, I. Gaballah, Kinetics of reduction of iron oxides by H_2. Part I: low temperature reduction of hematite, Thermochim. Acta 447 (2006) 89–100, doi:10.1016/j.tca.2005.10.004.
[40] A. Pineau, N. Kanari, I. Gaballah, Kinetics of reduction of iron oxides by H_2. Part II. Low temperature reduction of magnetite, Thermochim. Acta 456 (2007) 75–88, doi:10.1016/j.tca.2007.01.014.

[41] R.D. Walker, D.L. Carpenter, Influence of reducing gas composition on the structure and reducibitlity of iron oxides, J. Iron Steel Inst 208 (1970) 67.
[42] H. Kister, U. Pückoff, H.J. Engell, Einfluß von Wasserstoffzusätzen zu Kohlenmonoxidhaltigen Gas-Gemischen auf die Reduktion von Wüstit, Arch Eisenhuettenwes 43 (1972) 737–745, doi:10.1002/srin.197204457.
[43] H.-B. Zuo, C. Wang, J.-J. Dong, K.-X. Jiao, R.-S Xu, Reduction kinetics of iron oxide pellets with H_2 and CO mixtures, Int. J. Miner. Metall. Mater. 22 (2015) 688–696, doi:10.1007/s12613-015-1123-x.
[44] Q.T. Tsay, W.H. Ray, J. Szekely, The modeling of hematite reduction with hydrogen plus carbon monoxide mixtures: part I. The behavior of single pellets, AIChE J. 22 (1976) 1064–1072, doi:10.1002/aic.690220617.
[45] E. Kawasaki, J. Sanscrainte, T.J. Walsh, Kinetics of reduction of iron oxide with carbon monoxide and hydrogen, AIChE J. 8 (1962) 48–52, doi:10.1002/aic.690080114.
[46] D. Wagner, O. Devisme, F. Patisson, D. Ablitzer, A laboratory study of the reduction of iron oxides by hydrogen, in: Proceedings of the TMS Fall Extraction Processing Division Sohn International Symposium, 2006, pp. 111–120.
[47] K. Piotrowski, K. Mondal, H. Lorethova, L. Stonawski, T. Szymański, T. Wiltowski, Effect of gas composition on the kinetics of iron oxide reduction in a hydrogen production process, Int. J. Hydrog. Energy. 30 (2005) 1543–1554, doi:10.1016/j.ijhydene.2004.10.013.
[48] K. Piotrowski, K. Mondal, T. Wiltowski, P. Dydo, G. Rizeg, Topochemical approach of kinetics of the reduction of hematite to wüstite, Chem. Eng. J. 131 (2007) 73–82, doi:10.1016/j.cej.2006.12.024.
[49] Y.D. Wang, X.N. Hua, C.C. Zhao, T.T. Fu, W. Li, W. Wang, Step-wise reduction kinetics of Fe_2O_3 by CO/CO_2 mixtures for chemical looping hydrogen generation, Int. J. Hydrog. Energy 42 (2017) 5667–5675, doi:10.1016/j.ijhydene.2017.01.159.
[50] D.H.S. John, P.C. Hayes, Microstructural features produced by the reduction of wustite in H_2/H_2O gas mixtures, Metall. Trans. B 13 (1982) 117–124, doi:10.1007/BF02666962.
[51] D.H.S. John, S.P. Matthew, P.C. Hayes, The breakdown of dense iron layers on wustite in CO/CO_2 and H_2/H_2O systems, Metall. Trans. B 15 (1984) 701–708, doi:10.1007/BF02657292.
[52] M. Bahgat, Y. Sasaki, S. Hijino, M. Iguchi, K. Ishii, The effect of grain boundaries on iron nucleation during wüstite reduction process, ISIJ Int. 44 (2004) 2023–2028, doi:10.2355/isijinternational.44.2023.
[53] M. Bahgat, M.H. Khedr, Reduction kinetics, magnetic behavior and morphological changes during reduction of magnetite single crystal, Mater. Sci. Eng. B 138 (2007) 251–258, doi:10.1016/j.mseb.2007.01.029.
[54] Y. Sasaki, M. Bahgat, M. Iguchi, K. Ishii, The preferable growth direction of iron nuclei on wüstite surface during reduction, ISIJ Int. 45 (2005) 1077–1083, doi:10.2355/isijinternational.45.1077.
[55] S. El Moujahid, A. Rist, The nucleation of iron on dense wustite: a morphological study, Metall. Trans. B 19 (1988) 787–802, doi:10.1007/BF02650198.
[56] R. Nicolle, A. Rist, The mechanism of whisker growth in the reduction of wüstite, Metall. Trans. B 10 (1979) 429–438, doi:10.1007/BF02652516.
[57] C. Wagner, Mechanism of the reduction of oxides and sulphides to metals, JOM 4 (1952) 214–216, doi:10.1007/bf03397678.
[58] M. Farren, S.P. Matthew, P.C. Hayes, Reduction of solid wustite in $H_2/H_2O/CO/CO_2$ gas mixtures, Metall. Trans. B 21 (1990) 135–139, doi:10.1007/BF02658125.
[59] D.H.S. John, S.P. Matthew, P.C. Hayes, Establishment of product morphology during the initial stages of wustite reduction, Metall. Trans. B 15 (1984) 709–717, doi:10.1007/BF02657293.
[60] E.T. Turkdogan, R.G. Olsson, J.V. Vinters, Gaseous reduction of iron oxides: part II. Pore characteristics of iron reduced from hematite in hydrogen, Metall. Mater. Trans. B 2 (1971) 3189–3196, doi:10.1007/bf02814971.
[61] E.T. Turkdogan, J.V. Vinters, Gaseous reduction of iron oxides: part III, Met. Trans. 3 (1972) 1561–1574, doi:10.1007/BF02643047.
[62] M. Ettabirou, B. Dupré, C. Gleitzer, Nucleation and early growth of magnetite on synthetic and natural hematite crystals, React. Solids 1 (1986) 329–343, doi:10.1016/0168-7336(86)80025-0.
[63] F. Adam, B. Dupre, C. Gleitzer, Cracking of hematite crystals during their low-temperature reduction into magnetite, Solid State Ionics 32–33 (1989) 330–333, doi:10.1016/0167-2738(89)90237-3.
[64] S. Geva, M. Farren, D.H.S. John, P.C. Hayes, The effects of impurity elements on the reduction of wustite and magnetite to iron in CO/CO_2 and H_2/H_2O gas mixtures, Metall. Trans. B 21 (1990) 743–751, doi:10.1007/BF02654253.
[65] J. Takada, M. Adachi, Determination of diffusion coefficient of oxygen in α-iron from internal oxidation measurements in Fe-Si alloys, J. Mater. Sci. 21 (1986) 2133–2137, doi:10.1007/BF00547959.
[66] R. Barlow, P.J. Grundy, The determination of the diffusion constants of oxygen in nickel and α-iron by an internal oxidation method, J. Mater. Sci. 4 (1969) 797–801, doi:10.1007/BF00551075.
[67] H. Hagi, Diffusion coefficient of hydrogen in iron without trapping by dislocations and impurities, Mater. Trans. JIM 35 (1994) 112–117, doi:10.2320/matertrans1989.35.112.
[68] P. Pourghahramani, E. Forssberg, Reduction kinetics of mechanically activated hematite concentrate with hydrogen gas using nonisothermal methods, Thermochim. Acta 454 (2007) 69–77, doi:10.1016/j.tca.2006.12.023.
[69] A.A. Barde, J.F. Klausner, R. Mei, Solid state reaction kinetics of iron oxide reduction using hydrogen as a reducing agent, Int. J. Hydrog. Energy (2016) 10103–10119, doi:10.1016/j.ijhydene.2015.12.129.
[70] S.K. El-Rahaiby, Y.K. Rao, The kinetics of reduction of iron oxides at moderate temperatures, Metall. Trans. B 10 (1979) 257–269, doi:10.1007/BF02652470.
[71] S. Hayashi, Y. Iguchi, Morphology of iron reduced from wustite with H_2-H_2O-H_2S mixtures, ISIJ Int. 29 (1989) 596–604, doi:10.2355/isijinternational.29.596.
[72] C. Feilmayr, A. Thurnhofer, F. Winter, H. Mali, J. Schenk, Reduction behavior of hematite to magnetite under fluidized bed conditions, ISIJ Int. 44 (2004) 1125–1133, doi:10.2355/isijinternational.44.1125.
[73] M. Martin, Diffusion in oxides, in: Proceedings of the Diffusion in Condensed Matterials Methods, 2005, pp. 209–247, doi:10.1007/3-540-30970-5_5.
[74] A.A. El-Geassy, K.A. Shehata, S.Y. Ezz, Mechanism of iron oxide reduction with hydrogen/carbon monoxide mixtures, Trans. Iron Steel Inst. Jpn. 17 (1977) 629–635.
[75] A. El-Amir, F.M. Mohamed, S.T. Abdel-Rahim, M.E.H. Shalabi, Kinetics of direct reduction of el-baharia iron ore (el-gedida) oasis egypt, briquette via hydrogen, Int. J. Sci. Eng. Res. 6 (2015) 1018–1027.
[76] O.A. Teplov, Kinetics of the low-temperature hydrogen reduction of magnetite concentrates, Russ. Metall. 2012 (2012) 8–21, doi:10.1134/S0036029512010132.
[77] O.A. Teplov, Kinetics of the low-temperature hydrogen reduction of single-crystal magnetite, Russ. Metall. 2010 (2010) 991–1000, doi:10.1134/S0036029510110017.
[78] P. Chaurand, J. Rose, V. Briois, L. Olivi, J.L. Hazemann, O. Proux, J. Domas, J.Y. Bottero, Environmental impacts of steel slag reused in road construction: a crystallographic and molecular (XANES) approach, J. Hazard. Mater. 139 (2007) 537–542, doi:10.1016/j.jhazmat.2006.02.060.
[79] H. Motz, J. Geiseler, Products of steel slags an opportunity to save natural resources, Waste Manag. 21 (2001) 285–293, doi:10.1016/S0956-053X(00)00102-1.
[80] C. Pohlmann, L. Röntzsch, F. Heubner, T. Weißgärber, B. Kieback, Solid-state hydrogen storage in hydralloy-graphite composites, J. Power Sources 231 (2013) 97–105, doi:10.1016/j.jpowsour.2012.12.044.
[81] F. Adam, F. Jeannot, B. Dupre, C. Glettzer, The remarkable effect of water vapour on the cracking of hematite during its reduction into magnetite, React. Solids 5 (1988) 115–127, doi:10.1016/0168-7336(88)80081-0.
[82] B. Weiss, J. Sturn, F. Winter, J.L. Schenk, Empirical reduction diagrams for reduction of iron ores with H_2 and CO gas mixtures considering non-stoichiometries of oxide phases, Ironmak. Steelmak. 36 (2009) 212–216, doi:10.1179/174328108X380645.
[83] K. Higuchi, R.H. Heerema, Influence of sintering conditions on the reduction behavior of pure hematite compacts, Miner. Eng. 16 (2003) 463–477, doi:10.1016/S0892-6875(02)00180-2.
[84] K. Higuchi, R.H. Heerema, Influence of artificially induced porosity on strength and reduction behavior of hematite compacts, ISIJ Int. 45 (2005) 574–581, doi:10.2355/isijinternational.45.574.
[85] M.S. Valipour, M.Y. Motamed Hashemi, Y. Saboohi, Mathematical modeling of the reaction in an iron ore pellet using a mixture of hydrogen, water vapor, carbon monoxide and carbon dioxide: an isothermal study, Adv. Powder Technol. 17 (2006) 277–295, doi:10.1163/156855206777213375.
[86] F. Patisson, O. Mirgaux, Hydrogen Ironmaking: How it Works, Metals 10 (7) (2006) 922, doi:10.3390/met10070922.
[87] W. Mao, W.G. Sloof, Reduction kinetics of wüstite scale on pure iron and steel sheets in Ar and H_2 gas mixture, Metall. Mater. Trans. B 48 (2017) 2707–2716, doi:10.1007/s11663-017-1037-2.
[88] A.A. El-Geassy, Gaseous reduction of MgO-doped Fe_2O_3 compacts with carbonmonoxide at 1 173–1 473K, ISIJ Int. 36 (1996) 1328–1337, doi:10.2355/isijinternational.36.1328.
[89] K.C. Sabat, R.K. Paramguru, B.K. Mishra, Reduction of oxide mixtures of (Fe_2O_3 + CuO) and (Fe_2O_3 + Co_3O_4) by low-temperature hydrogen plasma, Plasma Chemistry Plasma Processing 37 (2017) 979–995, doi:10.1007/s11090-017-9818-6.
[90] M. Bachhav, F. Danoix, B. Hannoyer, J.M. Bassat, R. Danoix, Investigation of O-18 enriched hematite (α-Fe_2O_3) by laser assisted atom probe tomography, Int. J. Mass Spectrom. 335 (2013) 57–60, doi:10.1016/j.ijms.2012.10.012.
[91] B. Gault, D.W. Saxey, M.W. Ashton, S.B. Sinnott, A.N. Chiaramonti, M.P. Moody, D.K. Schreiber, Behavior of molecules and molecular ions near a field emitter, N. J. Phys. 18 (2016) 1–38, doi:10.1088/1367-2630/18/3/033031.
[92] H.J.T. Ellingham, Reducibilty of oxides and sulphides in metallurgical processes, J. Soc. Chem. Ind. 63 (1944) 33–64, doi:10.1002/jctb.5000630201.
[93] W.T. Du, I.H. Jung, Critical evaluation and thermodynamic modeling of the Fe–V–O (FeO–Fe_2O_3–VO–V_2O_3–VO_2–V_2O_5) system, Calphad 67 (2019) 101682 Comput. Coupling Phase Diagrams Thermochemhttps://doi.org/, doi:10.1016/j.calphad.2019.101682.
[94] K.E. Bullen, The Fe_2O Theory of Planetary Cores, in: Proceedings of the Continuum Mechanics Aspects of Geodynamics and Rock Fracture Mechanics, Netherlands, Springer, 1974, pp. 23–28, doi:10.1007/978-94-010-2268-2_3.
[95] S. Huang, X. Wu, S. Qin, Stability and anisotropy of $(Fe_xNi_{1-x})_2O$ under high pressure and implications in Earth's and super-Earths' core, Sci. Rep. 8 (2018) 1–8, doi:10.1038/s41598-017-18678-z.
[96] W. Guo, Y. Zhou, X. Sang, D.N. Leonard, J. Qu, J.D. Poplawsky, Atom Probe tomography unveils formation mechanisms of wear-protective tribofilms by ZDDP, ionic liquid, and their combination, ACS Appl. Mater. Interfaces 9 (2017) 23152–23163, doi:10.1021/acsami.7b04719.
[97] D. Zanuttini, I. Blum, L. Rigutti, F. Vurpillot, J. Douady, E. Jacquet, P.M. Anglade, B. Gervais, Simulation of field-induced molecular dissociation in atom-probe tomography: identification of a neutral emission channel, Phys. Rev. A 95 (2017), doi:10.1103/PhysRevA.95.061401.

[98] O.H. Gellner, F.D. Richardson, Reduction of ferrous oxide, Nature 168 (1951) 23–24, doi:10.1038/168023a0.
[99] H. Wang, H.Y. Sohn, Hydrogen reduction kinetics of magnetite concentrate particles relevant to a novel flash ironmaking process, Metall. Mater. Trans. B Process Metall. Mater. Process. Sci. 44 (2013) 133–145, doi:10.1007/s11663-012-9754-z.
[100] H. Wang, H.Y. Sohn, Effects of reducing gas on swelling and iron whisker formation during the reduction of iron oxide compact, Steel Res. Int. 83 (2012) 903–909, doi:10.1002/srin.201200054.
[101] A. Cores, A. Babich, M. Muñiz, S. Ferreira, J. Mochon, The influence of different iron ores mixtures composition on the quality of sinter, ISIJ Int. 50 (2010) 1089–1098, doi:10.2355/isijinternational.50.1089.
[102] Z. Chen, C. Zeilstra, J. van der Stel, J. Sietsma, Y. Yang, Review and data evaluation for high-temperature reduction of iron oxide particles in suspension, Ironmak. Steelmak. (2019) 1–7, doi:10.1080/03019233.2019.1589755.
[103] Y. Kapelyushin, X. Xing, J. Zhang, S. Jeong, Y. Sasaki, O. Ostrovski, Effect of alumina on the gaseous reduction of magnetite in CO/CO_2 gas mixtures, Metall. Mater. Trans. B 46 (2015) 1175–1185, doi:10.1007/s11663-015-0316-z.
[104] T. Paananen, K. Kinnunen, EFfect of TiO_2-content on reduction of iron ore agglomerates, Steel Res. Int. 80 (2009) 408–414, doi:10.2374/SRI09SP023.
[105] W.D. Tang, S.T. Yang, X.X. Xue, Effect of Cr_2O_3 addition on oxidation induration and reduction swelling behavior of chromium-bearing vanadium titanomagnetite pellets with simulated coke oven gas, Int. J. Miner. Metall. Mater. 26 (2019) 963–972, doi:10.1007/s12613-019-1813-x.